Journal of South American Earth Sciences 103 (2020) 102750

Contents lists available at ScienceDirect

Journal of South American Earth Sciences

journal homepage: www.elsevier.com/locate/jsames

Quartz textural analysis from an anastomosing shear zone system: Implications for the tectonic evolution of the Ribeira belt, Brazil

T. Conte [a,*], C. Cavalcante [a,b], L.E. Lagoeiro [a], H. Fossen [c], C.S. Silveira [a]

[a] UFPR – Federal University of Paraná, Department of Geology, Av. Cel. Francisco Heráclito dos Santos, 100, 81531-980, Curitiba, PR, Brazil
[b] UiT – University of Tromsø, The Arctic University of Norway, Department of Geosciences, Dramsveien 201, 9037, Tromsø, Norway
[c] UiB – University of Bergen, Museum of Natural History, Allégaten 41, 5007, Bergen, Norway

ARTICLE INFO

Keywords:
Textural analysis
Deformation mechanisms
Strain partitioning
Ribeira belt
Microstructures

ABSTRACT

Strain localization and influence of grain-size reduction processes were investigated from field and microstructural observations, and from quartz textural analysis using EBSD, in rocks deformed along an anastomosing network of shear zones in the Ribeira belt in Brazil. Rocks deformed along the Lancinha shear zone (LSZ) display high percentage of recrystallized grains, in which quartz recrystallized grain size from rocks in the southern LSZ reaches a maximum of 50 μm, and in the northern LSZ a maximum of 200 μm. The dominant serrated grain boundaries and the widespread (50–85%) presence of very small (>10–50 μm) recrystallized quartz grains, suggest that BLG was the dominant recrystallization mechanism responsible for grain-size reduction in the south portion of the LSZ. In the northern LSZ the presence of large recrystallized grains with sizes close to subgrains, suggests that grain-size reduction occurred by SGR, and the presence of lobate grain boundaries point to GBM recrystallization, which led to an increase in recrystallized grain size. This suggests grain-size reduction by dynamic recrystallization as a major factor leading to weakening and strain localization. Evidence of intracrystalline deformation and the well-developed quartz crystallographic fabrics suggest that strain localization in the LSZ occurred by dislocation creep deformation mechanisms. Dislocation creep is recorded by dominant activation of basal <a> slip and secondary contribution of rhomb <a> slip, in the southeast of the LSZ, and by activation of rhomb <a> + basal <a> and prism <a> in the northeast. These slip systems together with microstructural observations suggest that plastic deformation occurred at around 400 °C in the southern region, and at around at >400–500 °C in the northern region. S–C foliation, quartz <c> axis distribution and several kinematic indicators suggest sinistral sense of shear along the LSZ, and strain partitioning during progressive deformation. The dominance of sinistral indicators observed in the LSZ are also found in parallel shear zones to the east, such as the Putunã and Serra do Azeite. The sinistral kinematics in this overall dextral transpressional orogenic system may be explained by dual sense of shear on shear zones bounding extruding blocks, likely formed during progressive orogenic evolution instead of the polyphase evolution previously suggested for this southern part of the Ribeira belt.

1. Introduction

Shear zones are known as narrow zones that localize lithospheric deformation (Ramsay, 1980). Anastomosing shear zone systems represent mature stages of development that often record long progressive deformation histories. Many are associated with orogenic belts, such as the >900 km long and ~170 km wide anastomosing shear zone network found in the Ribeira belt that developed from 600 to 520 Ma, during the Brasiliano/Pan-African orogeny (Bento dos Santos et al., 2015; Machado et al., 2016). Exploring such shear zone systems and the way they accommodate deformation is important for our comprehension of crustal rheology and the way crust reacts to plate-scale deformation, and requires investigations at a range of scales and with different techniques.

Rocks in deforming shear zones typically undergo grain-size reduction processes by both brittle and plastic deformation mechanisms, the latter usually involving dynamic recrystallization. In general, such processes decrease the mechanical strength of rocks (Poirier, 1980; Hobbs et al., 1990; Platt and Behr, 2011), resulting in further localization of shear deformation as strain accumulates. Such localization potentially promotes strain partitioning from the microscale to that of an

* Corresponding author.
E-mail address: thailliconte@gmail.com (T. Conte).

https://doi.org/10.1016/j.jsames.2020.102750
Received 3 March 2020; Received in revised form 18 June 2020; Accepted 9 July 2020
Available online 18 July 2020

orogenic belt, producing tectonic domains of contrasting structural style, strain and complexity, and is therefore important to understand.

In the southern Ribeira orogenic belt, the Lancinha shear zone (LSZ) may, together with the Cubatão and Além Paraíba-Pádua shear zones, represent a first-order continental shear zone system (e.g. Sadowski, 1991) that involved intense grain-size reduction from upper to lower crustal levels. Even though observations of overprinting relations, porphyroclast inclusion trails and universal-stage quartz c-axis diagrams have been used to define a series of short-lived deformation phases in this shear zone system (e.g. Faleiros et al., 2016), we consider it a result of progressive deformation, typical for large shear zone systems (e.g. Fossen and Cavalcante, 2017 and references therein). Structural complexity in terms of style and kinematics is commonly associated with strain partitioning at various scales (Fossen et al., 2019). Understanding this evolution requires a variety of methods and techniques. While traditional field-based research has been presented in several recent publications, integrating such results with modern textural analysis (e.g., Cavalcante et al., 2018) is missing in the southern Ribeira belt. Such an approach, which is essential for a better comprehension of the process and mechanisms that lead to strain localization, and consequently, crustal deformation, is required to better understand the nature role of the Lancinha shear zone in the Ribeira belt.

In this work, digital geological mapping using the FieldMove Clino and GisKit applications is integrated with detailed micro-scale characterization by means of optical microscopy and SEM-EBSD of selected samples along the LSZ in the South of Brazil. The aim is to investigate the relation between micro- and large-scale structures, kinematic structures, the deformation mechanisms controlling strain localization, and the relationship between grain-size reduction (dynamic recrystallization) and texture development in the orogenic-scale shear zone system of the Ribeira belt.

2. Geological setting and sample description

The southern Ribeira belt (Fig. 1) resulted from the convergence between the São Francisco, Congo and Paranapanema cratons during the amalgamation of west Gondwana, at ~600 Ma (Trompette, 2000). It is characterized by the occurrence of several mostly dextral NE-SW trending strike-slip shear zones in what is considered an overall transpressional orogenic setting (Ebert and Hasui, 1998). The LSZ, together with the Morro do Agudo, Ribeira, Putunã, Serra do Azeite among others shear zones, form part of the anastomosing interconnected shear zone system that characterizes the southern Ribeira belt (Fig. 2). The LSZ is a 150 km long NE-trending strike-slip shear zone, with kinematics often referred to as dextral (e.g. Passarelli et al., 2011; Faleiros et al., 2011, 2016), that separates the Apiaí and Curitiba terranes (Fig. 3) (e.g. James and Assumpção, 1996; Campanha, 2002).

Intriguingly, rocks along the Serra do Azeite and Putunã shear zones, that are oriented parallel to the LSZ (Fig. 2), exhibit kinematic indicators such as S–C foliation, σ−porphyroclasts, sigmoidal boudins (e.g. Dehler et al., 2000, 2007), and garnet porphyroblasts with σ−type strain shadows (e.g. Faleiros et al., 2011), all suggestive of sinistral ductile deformation. The Serra do Azeite is interpreted as a transtensional mylonitic shear zone (e.g. Dehler et al., 2000; Machado et al., 2007). K–Ar dating in hornblende and biotite from orthogneisses and in phlogopite from metasediments, provided ages respectively at 565 ± 39

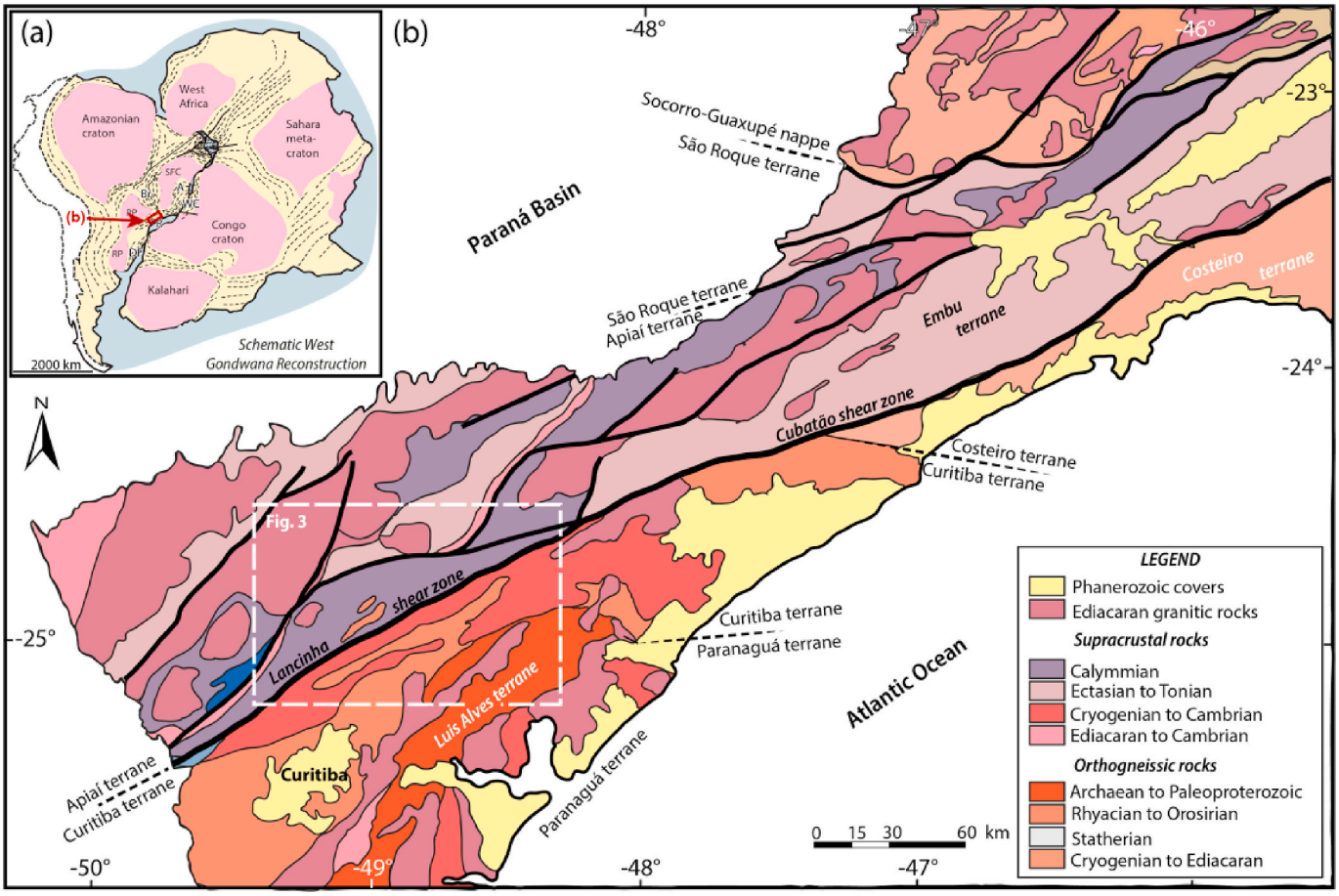

Fig. 1. **(a)** West Gondwana reconstruction with the main cratons (SFC-São Francisco craton; PP-Paranapanema; RP-Rio de la Plata) and orogenic belts (A-Araçuaí; R-Ribeira; WC-West Congo; DF- Dom Feliciano). **(b)** Geological map of the Ribeira belt showing the anastomosing shear zone network and the location of the study area (dashed box). Adapted from Campanha et al. (2015).

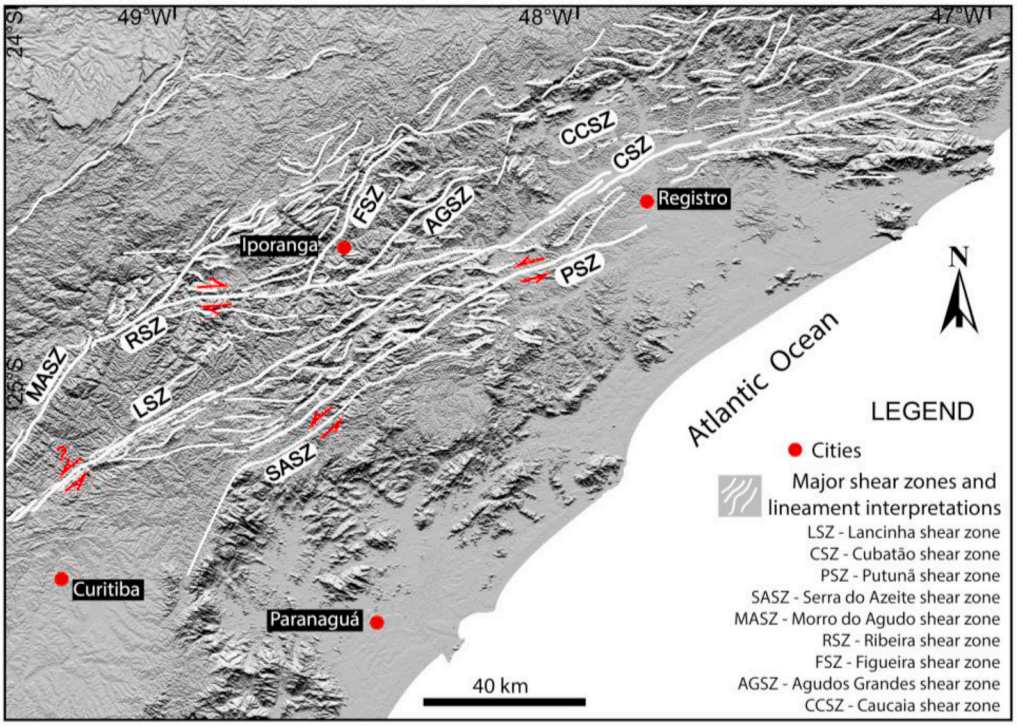

Fig. 2. Digital elevation model with lineament interpretations and major shear zones, displaying the interconnected pattern of shear zones in southern Ribeira belt. Available on http://www.webmapit.com.br/inpe/topodata/.

Ma, 527 ± 26 Ma and 587 ± 21 Ma, interpreted as minimum ages for the mylonitic deformation in the Serra do Azeite shear zone (Campagnoli, 1996). Furthermore, a muscovite K–Ar age of 577 ± 3 Ma was interpreted as the lower limit for the transtensional mylonitic deformation along the Serra do Azeite shear zone (Machado et al., 2007). Close to the study area, the Putunã shear zone is interpreted as a greenschist facies sinistral transcurrent shear zone (Faleiros et al., 2011). A chemical age of 579 ± 8 Ma obtained in monazite from a paragneiss was interpreted as a minimum age for the low temperature (greenschist facies) fabric developed along the Putunã shear zone (Faleiros et al., 2011).

The study area consists of the Apiaí and Curitiba terranes (Fig. 1). These terranes include low grade Neoproterozoic and Mesozoic metasedimentary rocks, and Paleoproterozoic to Archean gneissic and migmatitic units (Fig. 3). Deep weathering and limited amounts of outcrops make it difficult to define the LSZ in the study area, but most of the strain appears to be localized in a ≥200 m wide zone of sheared rocks. Generally, the rocks show a steep NE-SW to E-W trending foliation, monoclinal folds, slickenlines, S–C structures and a subhorizontal mineral stretching lineation.

Sampling was performed along four profiles with 66 outcrops across the Lancinha and Ribeira shear zones (Fig. 3). Six samples representative of the deformation related to the LSZ (Figs. 4 and 5) were selected for EBSD analysis and separated into two groups based on microstructural similarities and spatial distribution. One sample from the southernmost part of the LSZ, close to the Rio Branco town, which consists of phyllites with crenulation cleavage (Fig. 4a), did not provide reliable textural analysis data due to technical problems, and was therefore excluded from the CPO section (section 4.2).

Group 1 (G1), located in the southern portion of the LSZ, consists of quartzites (samples LC09H and LC59) with thin phyllosilicate-rich layers and mineral lineation characterized by elongated quartz grains (Fig. 4b and c), and of mylonitic granite (sample LC64B; Fig. 4e and f). Group 2 (G2), located in the northern portion of the LSZ (Fig. 3), consists of (garnet) schists (samples LC30C1 and LC30DSC) with mineral lineation characterized by shape preferred orientation of quartz grains, and with quartz ribbons with aspect ratio of about 1:5, associated with numerous deformed quartz veins (Fig. 5). They display S–C fabric indicating normal-sinistral sense of shear. These rocks belong to the Açungui Group and Atuba complex (Fig. 3).

3. Analytical methods

The thin sections were cut perpendicular to the foliation and parallel to the stretching lineation (XZ plane of the finite strain ellipsoid), followed by 3, 1 and 0.25 μm diamond paste polishing and colloidal silica in suspension polishing to remove surface damage. EBSD analysis was conducted with a FEG Quanta 450 and with a Tescan Mira3 LM field emission gun scanning electron microscopes, at the Electron Microscopy Centre (CEM) and at the Materials and Structures Laboratory (LAME) at the Lactec Institute, at the Paraná Federal University (UFPR), Brazil. Operating conditions were at 20 kV accelerating voltage, 15 mm of working distance, 70° specimen tilt, and a step-size ranging from 1.2 to 3.40 μm. An Oxford Nordlys Nano EBSD detector was used for measuring diffraction patterns, which were collected and indexed using the AZtec software from Oxford Instruments. An OIM Analysis™ software from EDAX instruments was also used for acquisition and treatment of EBSD patterns.

The acquired EBSD data were processed for texture analyses using the MTEX toolbox (Hielscher and Schaeben, 2008; Bachmann et al., 2010), version 4.5.0, for Matlab™, from which pole figures (PF), phase and Euler angle maps, inverse pole figures (IPF), and misorientation histograms were produced. Grain-size distribution histograms were produced using the CHANNEL 5 software from Oxford Instruments. To establish reliable correlations and comparisons, EBSD data from all samples have undergone a unique cleaning routine, where EBSD pixels with the mean angular deviation (MAD) higher than 1.2° and grains with less than 2 indexed points were excluded. Grain boundaries were defined at misorientation angle >10°. The grain-size distribution was calculated from EBSD orientation maps based on 2D area fraction, using weighted grain areas, with each grain having at least 100 pixels and

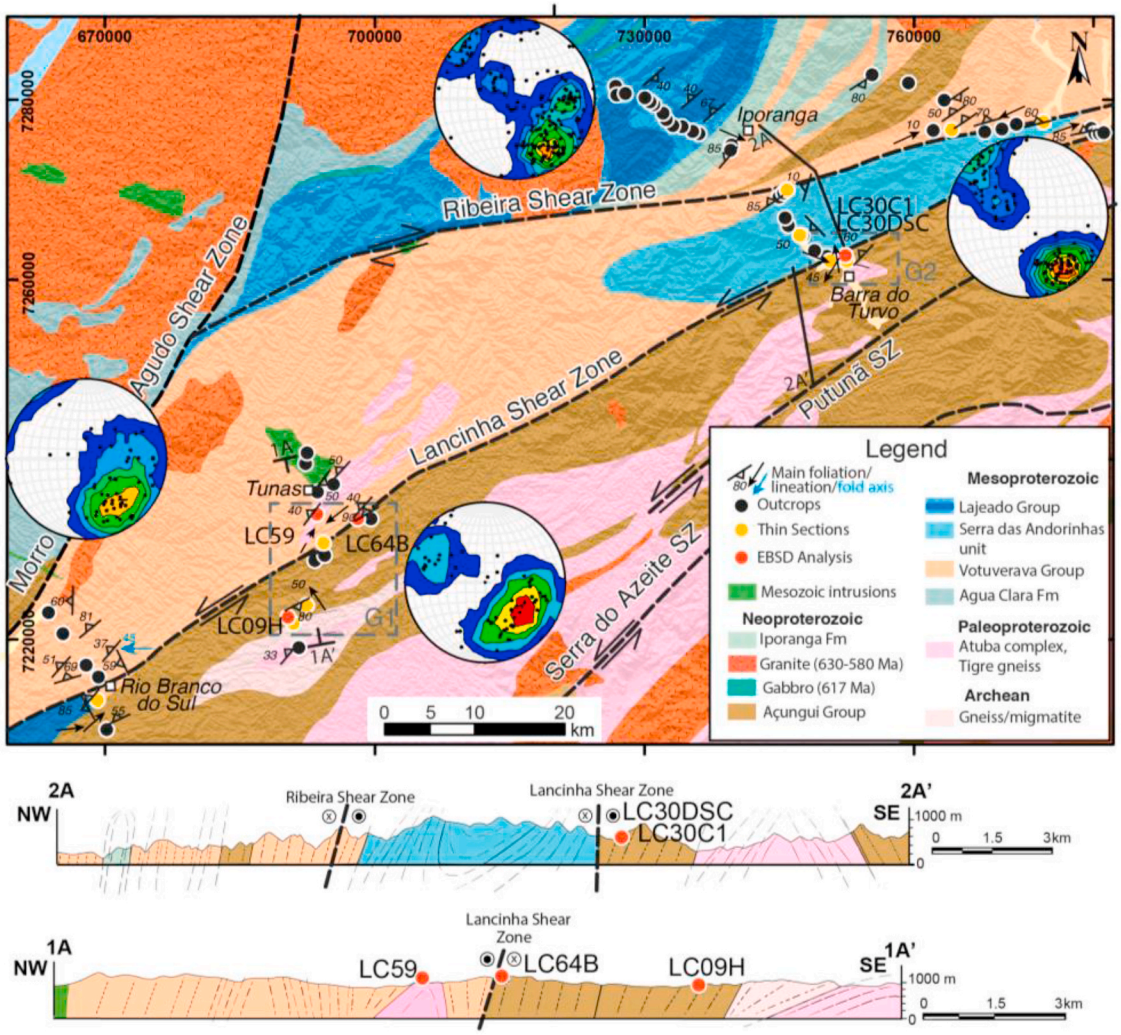

Fig. 3. Detailed geological map on a digital elevation model image of the study area, showing location of visited localities, samples selected for EBSD analysis, stereoplots for planar fabrics (foliation/cleavage), and schematic cross sections. Dashed boxes represent groups 1 and 2 (G1 and G2) samples, selected for EBSD analysis. Based on digital map by the Brazilian Geological Survey (http://geobank.cprm.gov.br/), Faleiros et al. (2012) and Faleiros and Pavan (2013).

samples having more than 500 grains (e.g. Herwegh, 2000; Berger et al., 2011; ASTM E2627-13, 2019). For each sample, [c], <a> directions, and poles for crystallographic planes {m}, {r}, and {z} in quartz were plotted.

4. Results

4.1. Fabric elements and microstructures

The most striking textural feature observed from a total of seventeen thin sections from the LSZ and adjacent areas (Fig. 3) is the microscale alternation of quartz- and mica-rich layers that defines an anastomosing foliation (Fig. 6a). Quartz layers consist of recrystallized asymmetric aggregates indicating sinistral sense of shear (Fig. 6b). Metasedimentary rocks from the Açungui Group also exhibit agglomerates of coarse quartz grains (0.3 mm diameter), often optically strain-free, or with weak undulose extinction and straight and irregular boundaries, among randomly oriented biotite grains, which reach up to 1 mm in size (Fig. 6c).

Quartz recrystallized grains from quartzites range in size from 10 to 50 μm. Schists have coarse-grained (50–200 μm) quartz, which occurs as recrystallized bands that, along with thin mica layers, commonly form a S–C fabric, which suggests sinistral sense of shear (Fig. 6d). Mica grains with fish geometry and garnet porphyroblasts also indicate sinistral sense of shear (Fig. 6d, e, f). Undulose extinction and deformation bands in mica often occur both in quartzites and schists. The schists also show mica kink bands (Fig. 6f).

4.1.1. Group 1 (G1) microstructures

This group (Fig. 3) is represented by quartzites (samples LC09H and LC59; Fig. 7a and b) and by granitoid with mylonitic foliation (sample LC64B). Quartzites are composed of inequigranular quartz aggregates and quartz ribbons (95%) and thin mica layers. Quartz grains with strongly flattened shapes have sizes ranging from 50 to 400 μm long (Fig. 7c). They often form wavy ribbons with an aspect ratio of 1:3 and sigma shapes, that together with thin layers of phyllosilicates, characterize the anastomosing foliation, locally arranged in a S–C geometry in which S consists of wavy elongated quartz and C of recrystallized quartz grains (Fig. 7c). Quartz often shows strong shape preferred orientation and serrated grain boundaries suggestive of bulging (BLG) recrystallization (Fig. 7c and d), few subgrains and few new grains with sizes close to the subgrain sizes, undulose extinction and deformation bands (Fig. 7e).

The mylonitic granitoid (sample LC64B) consists of quartz (50%), feldspar (40%) and phyllosilicates (10%). The mylonitic foliation is characterized by elongated quartz ribbons surrounding feldspar porphyroclasts (Fig. 7f). The feldspar porphyroclasts are strongly fractured. Very small grains consisting mostly of feldspar occur along their

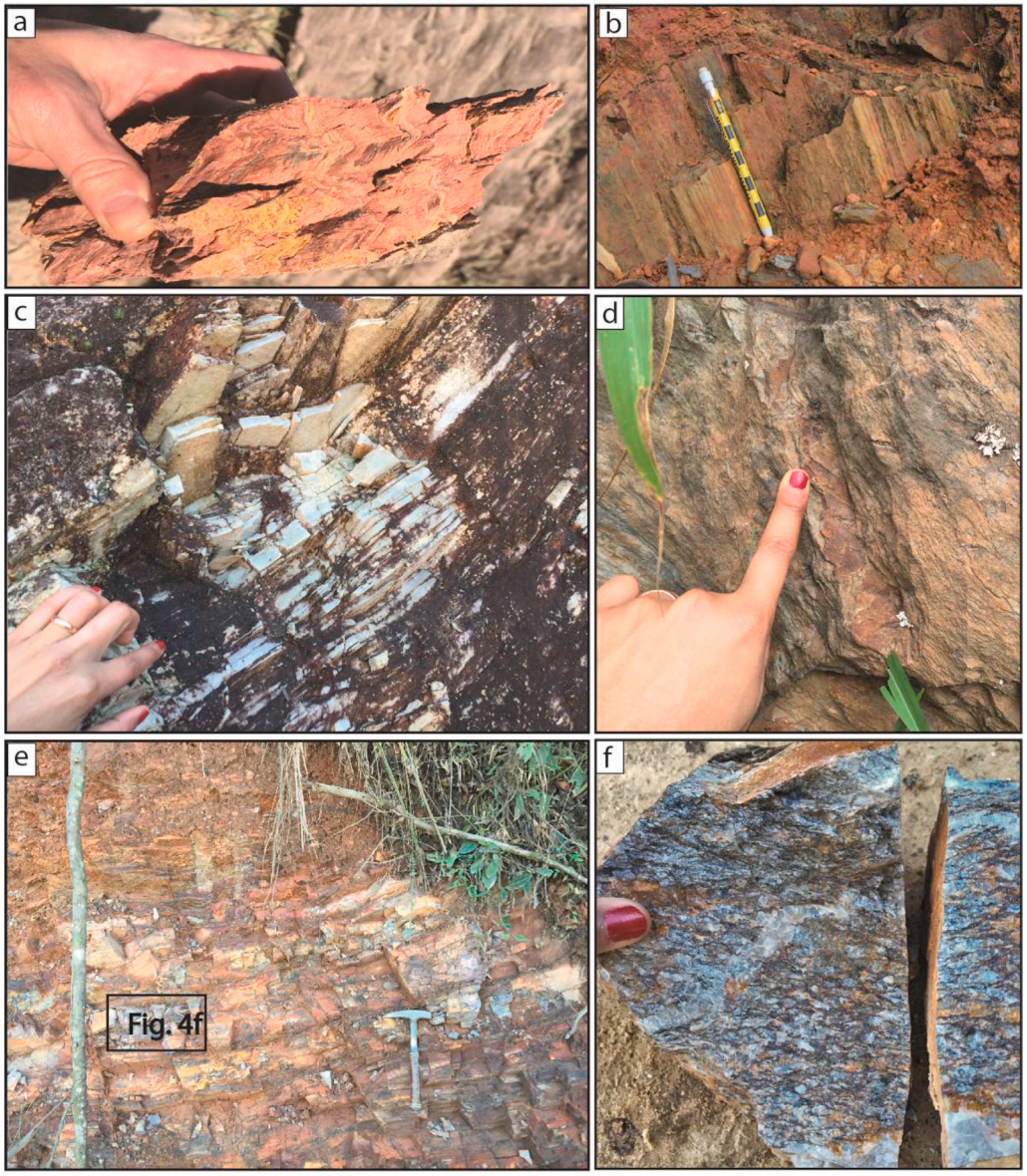

Fig. 4. Pictures of outcrops representative of the Group 1 rocks: **(a)** Phyllites with crenulation cleavage; **(b)** elongated quartz grains characterizing the stretching lineation in quartzite; **(c)** quartzite with steeply dipping foliation; **(d)** The continuous foliation of the phyllitic rocks; **(e)** mylonitic granite with sub-vertical foliation and; **(f)** detail of the mylonitic foliation in Fig. 4e.

fractures and margins (Fig. 7g), and such small feldspar grains, as compared to the parent grains, suggest recrystallization by BLG or result of classical nucleation (e.g. Fitz Gerald and Stünitz, 1993). Quartz grains with undulose extinctions and few subgrains sometimes display sigmoidal shape (~50 μm long); quartz ribbons have aspect ratio of ~1:4 and are often surrounded by small recrystallized grains (up to 10 μm in size), with serrated grain boundaries (Fig. 7h and i) typical of BLG recrystallization (e.g. Stipp et al., 2002b).

4.1.2. Group 2 (G2) microstructures

Samples from this group (LC30DSC and LC30C1) consist of (garnet) quartz-schist that contains strongly shape-oriented phyllosilicates (mainly biotite), K-feldspar, plagioclase, amphiboles and epidote. Quartz is abundant (70%) and occurs as: (i) recrystallized bands in which grain size ranges from 50 to 200 μm; (ii) strongly recrystallized grains in the matrix (Fig. 8a and b), with grain size ranging from >10 to 50 μm and boundaries mainly irregular serrated, suggestive of BLG recrystallization and; (iii) layers with subgrains/new grains oriented oblique to the foliation, suggestive of SGR recrystallization. Quartz also occurs as polycrystalline ribbons with aspect ratios of 1:7, commonly with lobate grain boundaries suggestive of grain boundary migration (GBM) recrystallization (Fig. 8c). Garnet porphyroblasts, reaching up to 5 mm in diameter, show quartz inclusions and recrystallized quartz in pressure shadows, indicating sinistral sense of shear (Fig. 8d). Biotite grains distributed in the matrix often characterize a S–C geometry and show undulose extinction and kink bands. Plagioclase grains show undulose extinction and deformation twinning and are surrounded by biotite with strong preferred orientation (Fig. 8e and f). Undulose extinction also occurs in amphibole grains that have sigmoidal shapes.

4.2. Crystallographic preferred orientation (CPO) - textural analysis

Quartz crystallographic orientations were measured in all samples from the two groups (G1 and G2). The selected EBSD areas are shown in Fig. 7a, b, f and Fig. 8a, b, and the pole figures (PF) and inverse pole figures (IPF) are presented in Fig. 9 and Fig. 10. The EBSD maps are available in the supplementary material. All PFs calculated from ODF (orientation distribution function) are shown with the foliation oriented

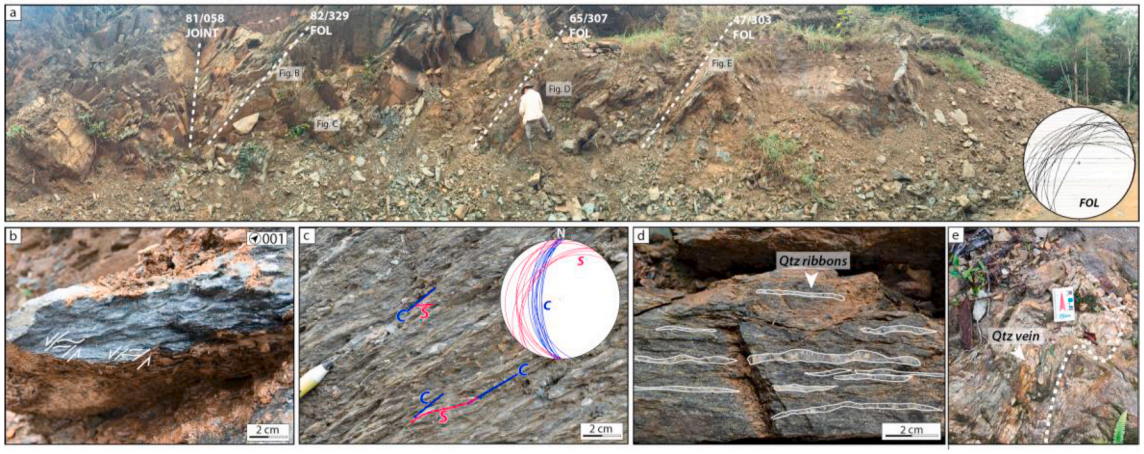

Fig. 5. **(a)** Picture of schist outcrop representative of Group 2 rocks. White dashed lines indicate the foliation and joint traces, and the stereoplot shows the orientation of the foliation; **(b)** and **(c)** S–C fabric indicating normal-sinistral sense of shear. The stereoplot displays the S and C orientations; **d)** quartz ribbons; **(e)** folded quartz vein.

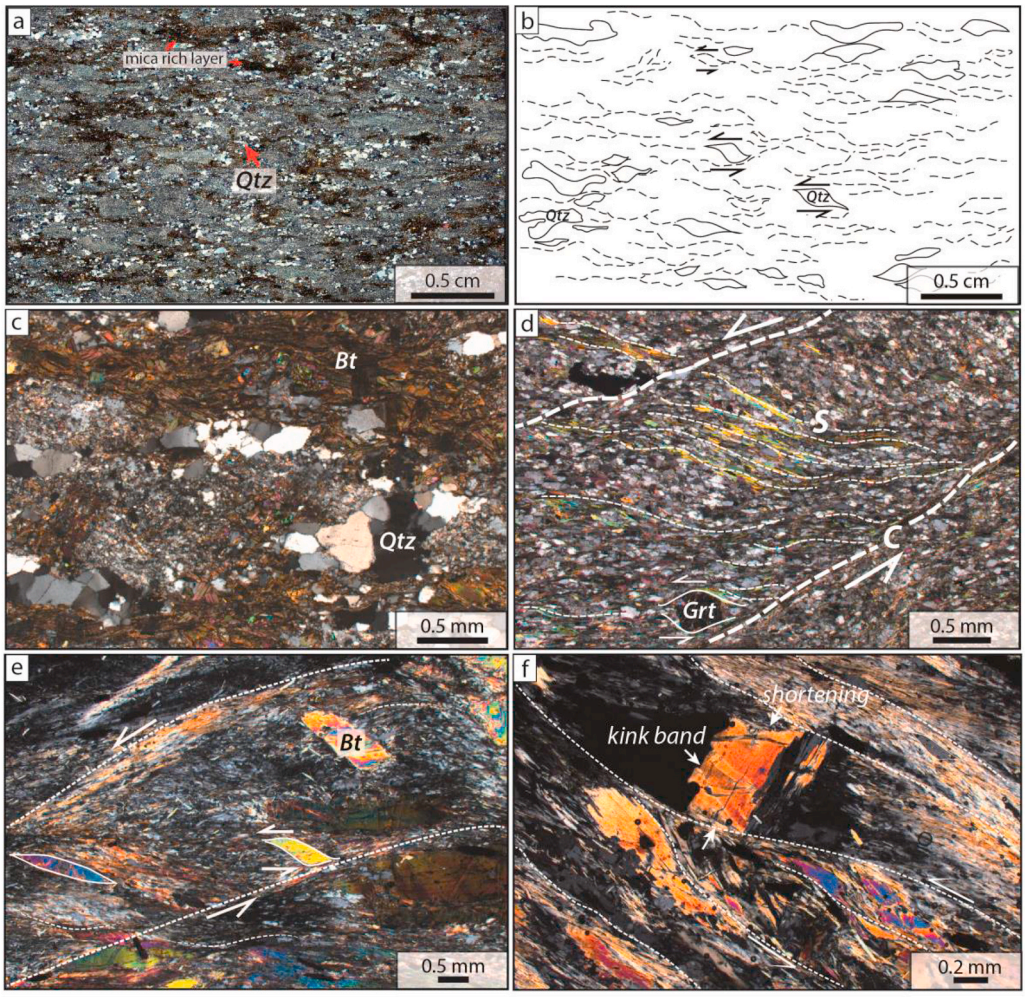

Fig. 6. Image of scanned thin sections (crossed polarizers) and optical photomicrographs of microstructures from representative rocks exposed along the Lancinha and correlated shear zones. (a) Alternating recrystallized quartz aggregates and muscovite-rich layers characterize the anastomosing foliation. Asymmetric shapes of quartz aggregates indicate sinistral sense of shear, highlighted in the sketch (b); (c) Strain-free and weakly deformed quartz grain agglomerates exhibiting straight and irregular boundaries, within fine-grained quartz-mica matrix; (d) S–C type of anastomosing foliation and rotated garnet porphyroblast indicating sinistral sense of shear in schists; (e) Biotite with fish geometry indicating sinistral sense of shear; (f) Biotite with kink bands as observed in schist.

E-W and vertical, and the lineation oriented E-W and horizontal, represent one point per grain measurement, and they all represent X-Z sections of the finite strain ellipsoid. Inference of active slip systems were based on the assumption that CPO skeletons or maxima result from the activity of dominant slip systems (e.g. Lister et al., 1978; Price, 1985).

4.2.1. Group 1 (G1) quartz crystallographic orientation

PFs from samples LC09H and LC59, both from quartzites, show a strong concentration of quartz c-axis at 15–30° counterclockwise to the pole of the foliation (Z) and <a> axis with a broad distribution along the foliation plane, with weak concentrations close to X, consistent with basal <a> slip (e.g. Little et al., 2013) and sinistral sense of shear

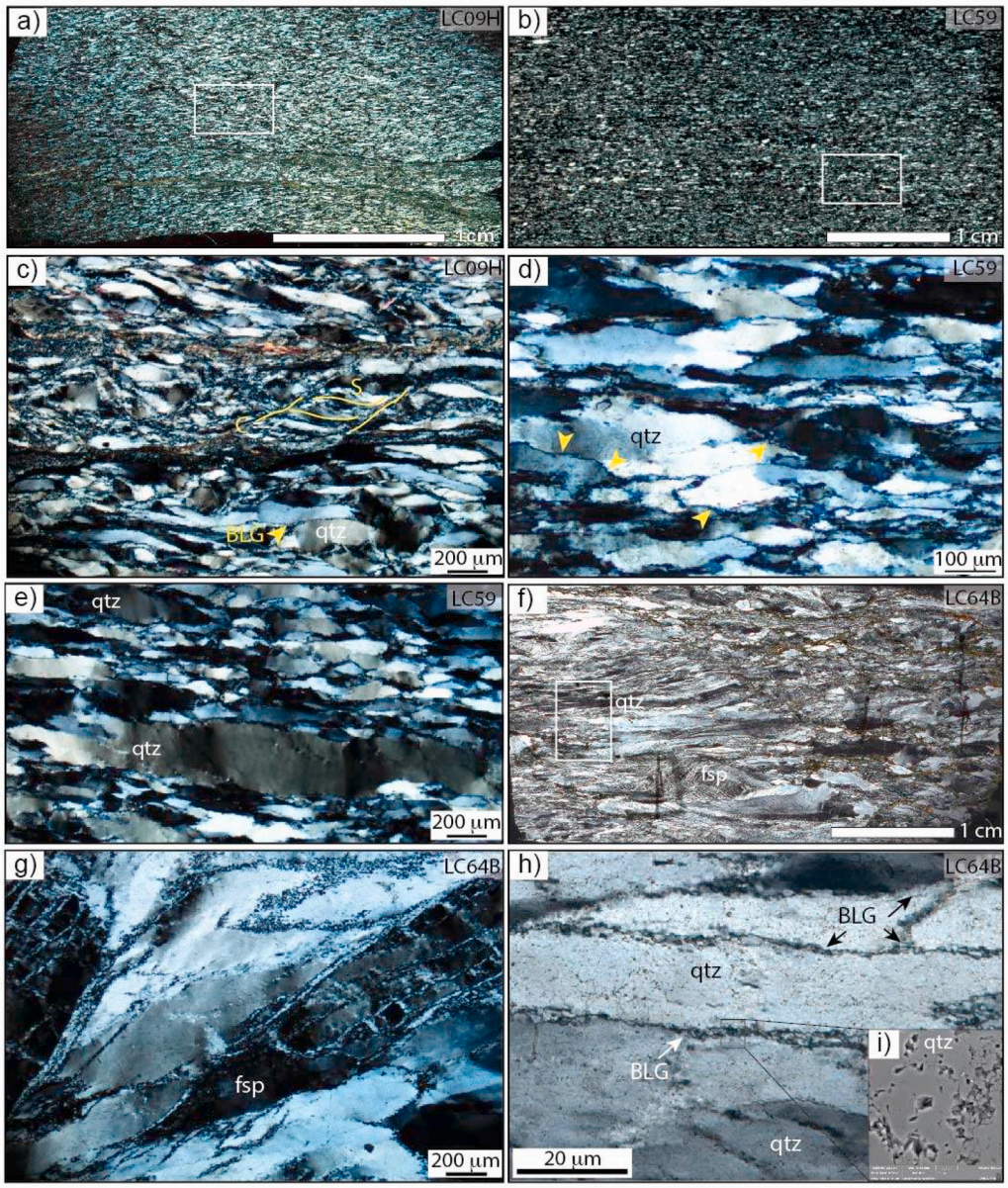

Fig. 7. Microstructures from rocks of the G1. (a) and (b) Scanned images of thin section with polarized light displaying the general aspects of quartzites; (c) Flattened quartz grains exhibiting sweeping undulatory extinction, arranged along an anastomosing foliation that locally forms a S–C geometry, and small quartz grains probably formed by BLG recrystallization, along grain boundaries (yellow arrow); (d) Elongated quartz grains exhibiting undulose extinction and serrated grain boundaries (yellow arrows) suggestive of BLG recrystallization; (e) quartz ribbons with undulose extinction, subgrains, and irregular serrated grain boundaries; (f) Image of scanned thin section (crossed polarizers) from sample LC64B displaying the general aspect of the mylonitic granite; (g) Fractured feldspar porphyroclast in the mylonitic granite, with very small grains occupying its fractures and margins; (h) Detailed photomicrography from sample LC64B showing recrystallized BLG domains at quartz serrated grain boundaries and; (i) BSE image displaying the very small (<10 µm) serrated quartz grain boundaries. White boxes in the scanned images are areas selected for EBSD analysis. (For interpretation of the references to color in this figure legend, the reader is referred to the Web version of this article.)

(Fig. 9). Poles to {m} planes are distributed along great circles with weak maxima close to X (LC09H) and Y (LC59) (Fig. 9). Rhomb planes {r} and {z} show a wide distribution with maxima with different strengths close to Z and X, and at high angle to X. Maxima close to Z point to some slip along rhomb {r} planes, a slip system also inferred from the IPF for sample LC09H (e.g. Schmid and Casey, 1986). Activation of both basal <a> and rhomb <a> together with evidence of dominant BLG recrystallization suggest quartz from quartzites deformed under low temperature conditions ≤400 °C (e.g. Stipp et al., 2002b).

Sample LC64B displays <c> axis distributed along a broad great circle that runs from northwest to southeast, with a small-circle maximum oblique to X (Fig. 9). <a> axis and poles to {m} show a similar texture that defines a broad great circle running from northwest to southeast, with a weak cluster at ≤30° (<a> axis) and close to X ({m} poles). {r} and {z} planes are quite dispersed, with small concentrations close to X and at ~30° clockwise to Z. Although {z} planes are oriented favorable for slip, activation of rhomb <a> is unlikely due to the <a> axis orientation being oblique to X.

G1 IPFs for X and Z directions show a gentle concentration of {m} and <a> close to the X direction, while <c> axis clearly concentrates close to Z, especially for the quartzites samples (LC09H and LC59), as well as some positive rhomb planes. Such a distribution reiterates the suggestion of the activation of basal <a> slip, with some contribution of rhomb <a> slip, especially for sample LC09H. For the mylonitic granite (LC64B), IPF and pole figures do not allow for a conclusive interpretation in terms of slip systems.

4.2.2. Group 2 (G2) quartz crystallographic orientation

The two areas (A1 and A2) selected for EBSD analysis (Fig. 8a) on sample LC30DSC display similar textures (Fig. 10). <c> axes display well-defined small circles located at the periphery oblique to the foliation, at ~30° counterclockwise to Z, consistent with sinistral sense of shear and basal <a> slip (e.g. Schmid and Casey, 1986; Mancktelow and Pennacchioni, 2004). <a> and poles to {m} are distributed along girdles normal to <c>, with strong concentrations close to X. Poles to rhomb {r} define a cleft girdle distribution according to Lister and Hobbs' (1980) classification. Poles to rhomb {z} define a crossed girdle for area A1 and three scattered maxima for area A2. IPF figures for this sample are concentrated around {m} and <a> for the X direction, and around <c> and {m} for the Z direction for areas A1 and A2, respectively. Such an

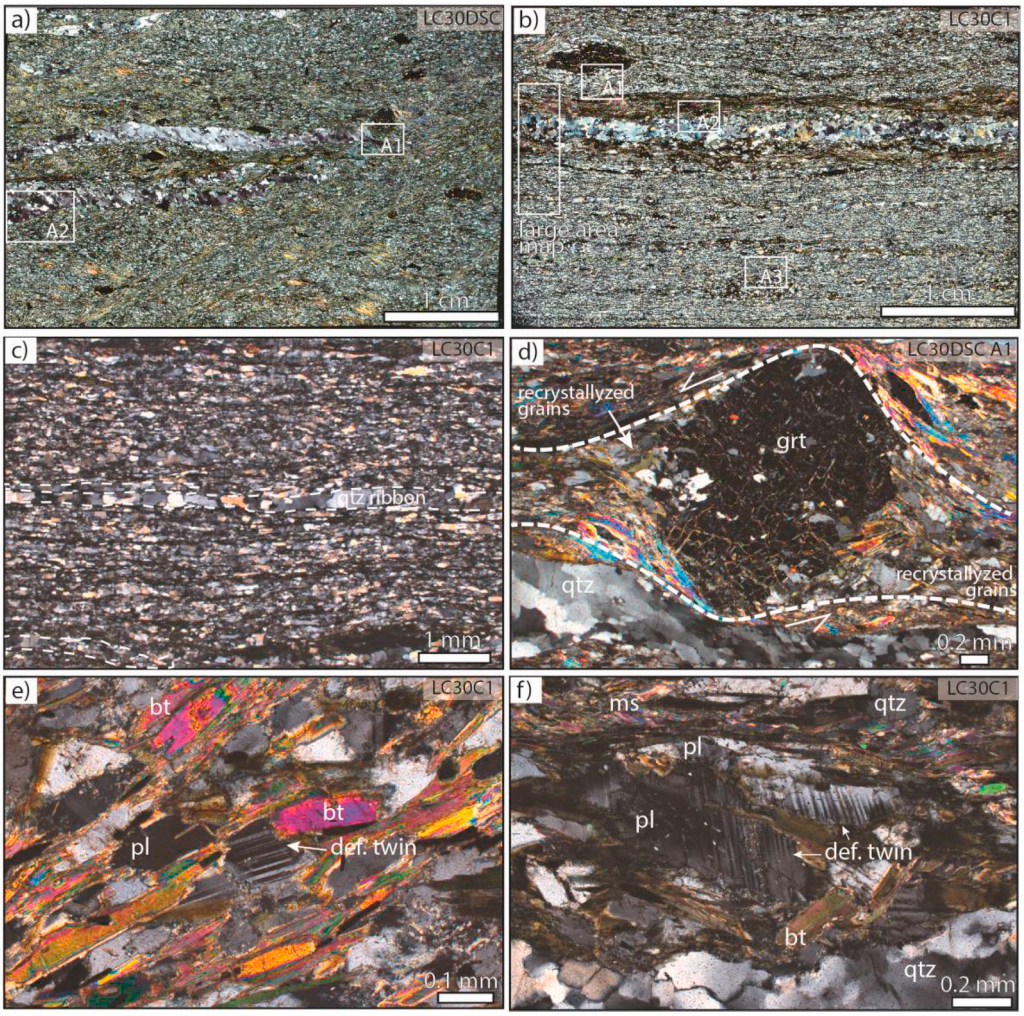

Fig. 8. Microstructures from rocks of the G2. (a) and (b) Image of scanned thin section with polarized light from quartz-schists showing the distribution of quartz grains in recrystallized bands and in the matrix (highlighted white boxes represent the selected areas for EBSD analysis); (c) Polycrystalline quartz ribbon exhibiting lobate grain boundaries; (d) Garnet porphyroblast with recrystallized quartz grains in pressure shadows indicating sinistral sense of shear, and quartz rich layer with oblique subgrains (lower part of the image); (e) and (f) Plagioclase grains with undulose extinction and deformation twins surrounded by biotite with strong preferred orientation (e) and arranged in a S–C fabric (upper right side in f).

IPF distribution, even if it is not clear, is still consistent with activation of basal <a> slip, and also with some prism {m} planes oriented favorable for slip.

Four areas were selected on sample LC30C1 (A1, A2, A3 and Large Area Map; Fig. 8b). Quartz from Area A1 display <c> axes distributed along a single narrow girdle that runs from northwest to southeast, at a small angle counterclockwise to Z, suggestive of sinistral sense of shear and some activity of basal <a> slip (Fig. 10). Poles to {m} and <a> exhibit similar texture with several maxima that define a few main concentrations close to X and at ~30° to X, respectively. Poles to rhomb {r} characterize a single narrow girdle that runs from north to south and a small circle close to X. Poles to rhomb {z} define a north-south cleft girdle (e.g. Little et al., 2013). IPFs display some grains with <a> axis oriented parallel to X and positive rhomb planes favorably oriented for slip, suggestive of rhomb <a> activity.

Quartz from Area A2 show <c> axis distribution forming several small oblique maxima that extend toward the center, almost defining a single girdle, with main maximum at ~20° counterclockwise to Z, suggesting sinistral sense of shear, basal <a> slip, and some rhomb slip (e.g. Heilbronner and Tullis, 2006, Fig. 10). Additional activation of rhomb <a> slip can also be suggested from the IPF map, which includes certain grains with rhomb {r} planes favorably oriented for slip and some grains with <a> axes close to X. <a> axes and poles to {m} are distributed along great circles normal to <c> axis main maximum. Poles to {r} are spread out, but weak maxima at ~20° to the lineation and close to Z can be observed. Poles to {z} define a diffuse cleft girdle, which runs from north to south.

Quartz from Area 3 displays <c> axis distributed along a broad girdle that runs from northeast to southwest at a small angle clockwise to Z, indicative of dextral sense of shear (Fig. 10). There are also indications of basal <a> and rhomb <a> slip, also noticeable from the IPF diagram, with <a> axes oriented parallel to X and rhomb and basal planes oriented favorable for slip. <a> and poles to {m} have similar texture with a wide distribution, although small maxima on the perimeter on either side of X occur. Poles to {r} present a wide distribution with three weak concentrations close to X and Z. Poles to {z} define a broad cleft girdle.

<c> axes are distributed along a single broad symmetric girdle that runs from north to south, with a strong concentration close to Y, pointing to an important activity of prism <a> slip (e.g. Schmid and Casey, 1986; Stipp et al., 2002a; Mancktelow and Pennacchioni, 2004) and a strong component of coaxial deformation. Poles to {m} and <a> axes show a rather scattered distribution with weak concentrations around X.

Poles to rhomb planes are also scattered, but some weak concentrations of {r} poles close to X and around Y and Z occur. Evidence of secondary activity of rhomb <a> slip in the IPFs, which display certain grains with <a> axis oriented parallel to X and rhomb forms favorably oriented for slip, is also observed. Poles to {z} define a sort of broad cleft girdle running from north to south.

4.2.3. *Grain size distribution (GSD)*

Grain size distribution for quartz from all samples is presented in Fig. 11. Quartz in quartzites from G1 have similar grain-size

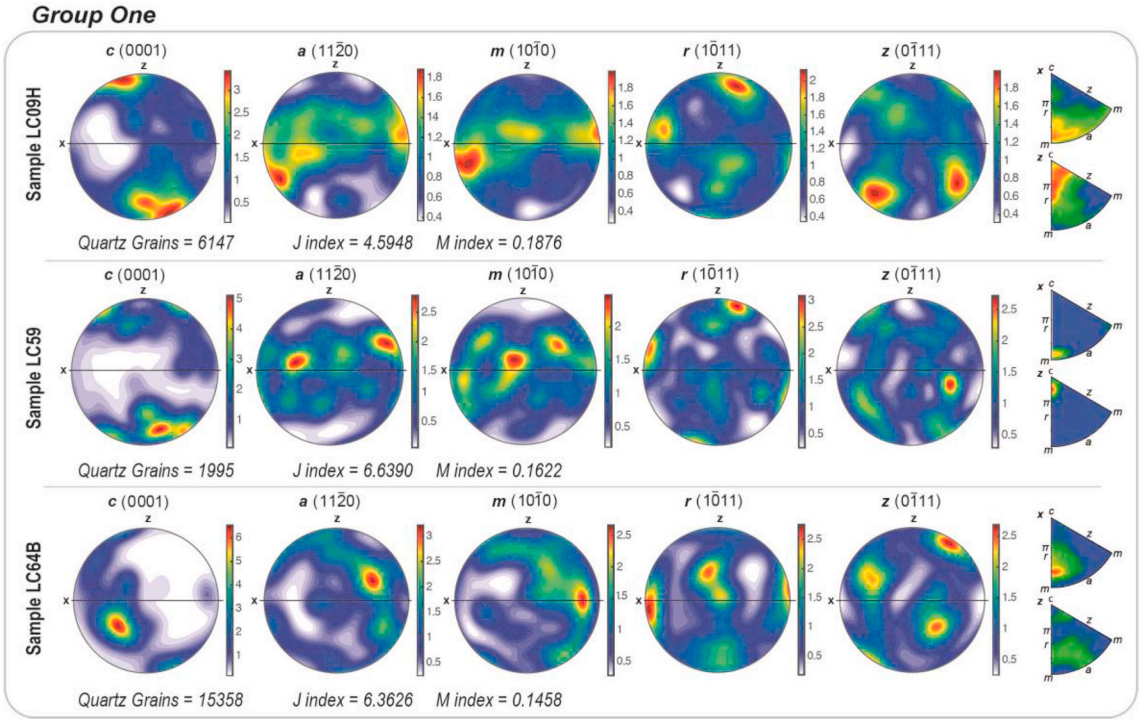

Fig. 9. Quartz crystallographic orientations for rocks from G1. Pole and Inverse pole figures (IPF). Pole figures are represented at lower hemisphere equal-area projections. IPFs are represented for X (upper right corner) and Z directions (lower right corner). The densities of poles diagrams were color-coded and contoured in Multiples of a Uniform Distribution (M.U.D.), defined by the scale bar on the right of each pole figure. (For interpretation of the references to color in this figure legend, the reader is referred to the Web version of this article.)

distribution, with ~50% of grains from the EBSD mapped area being up to 50 μm in diameter. These grains represent recrystallized grains. The main concentration of recrystallized grains occurs at >10–15 μm (20%) in sample LC09H, and at >35–40 μm (17%) in sample LC59. The percentage of recrystallized grains in the EBSD mapped area of the mylonitic granite (LC64B) is smaller than for the quartzites, consisting of ~35% of grains with up to 50 μm diameter. The main peak occurs at grains with >10–15 μm (18%).

Recrystallized quartz grains from the EBSD mapped area in schists from G2 reach 200 μm in size. Recrystallized grains with very small sizes (up to 50 μm) make up between 50 and 80% of the EBSD mapped area for both samples (LC30DSC and LC30C1). In the two areas in sample LC30DSC the percentage of recrystallized grains is ~90%. The main peaks of grain sizes occur at >10–15 μm for both areas, being 35% in LC30DSC - Area 1 and ~27% in LC30DSC – Area 2.

Recrystallized grains from the four areas in sample LC30C1 represent between 50 (Area 2) and 100% (Area 3) of the EBSD mapped area. LC30C1-Area 1, LC30C1-Area 2 and LC30C1-Area 3 have main grain size peaks at >10–15 μm (>20–25%). LC30C1-Large area map has two main grain-size peaks at >15–20 μm and at >10–15 μm (>20–25%).

4.2.4. Misorientation angle distribution

The misorientation angle distribution for quartz grains are represented in frequency histograms for G1 and G2 samples in Fig. 12. The angle of misorientation is the angle between one crystal lattice orientation and its neighbor and can be expressed by a rotation axis and rotation angle (Wheeler et al., 2001). The misorientation histograms were plotted from the mean grain orientation for grain segmentation with a minimum misorientation angle of 2°. Misorientation analysis of grain boundaries were performed for uncorrelated (random pairs) and correlated (neighbor pairs) distribution of angles.

Quartz misorientation angles histograms for all samples from G1 and G2 show one sharp peak at high angles close to 55–60° (except the LC59 from G1), associated with rotation axes in [0001], indicating the presence of Dauphiné Twinning (e.g. Neumann, 2000; Menegon et al., 2010; Wenk et al., 2011). Samples from G1 and LC30C1 (Area 3 and Large Area Map) and LC30DSC (Area 1) from G2 also display a secondary peak at <15°, which suggest the presence of some subgrain boundaries (e.g. Wheeler et al., 2001; Menegon et al., 2010). The rotation axes tend to be aligned parallel to [0001]. The histograms show also some high-angle boundaries in the interval between >15 and 100°, especially for G1 samples. All samples except the LC59 show maxima for the misorientation axes in the 60–65° range parallel to the c-axis, which could be related to activity of the prism slip system {m} < a >. However, in the pole figure plot (Figs. 9 and 10), some concentrations of c-axis around the Y-axis is only observed for sample LC30C1 (Area 1, Area 3 and Large Area Map) from G2. Thus, for all the other samples the misorientation axes in the 60–65° range parallel to the c-axis is again interpreted as indicative of Dauphiné twin boundaries. Additionally, most samples show uncorrelated misorientation angles between 20 and 50° with higher frequency than expected for a uniform distribution, whereas misorientation greater than 50° for both correlated and uncorrelated grains occur with a lower frequency than expected for a uniform distribution, in all samples.

5. Discussion

5.1. Interpretation of (micro) structures and CPO data

From field, microstructural observations and textural analysis (EBSD data) on rocks from two groups (G1 and G2) in the Lancinha shear zone and associated shear zones, four main characteristics can be highlighted: (1) intense grain-size reduction with recrystallized grains (up to 50 μm in G1 and up to 200 μm in G2) constituting between 50 and 100% of the EBSD mapped areas (Fig. 11) in most samples, except the sample LC64B mylonitic granite, which recrystallized grains make ~35%; (2) anastomosing foliation and S–C fabrics (Figs. 6 and 7), (3) widespread presence of Dauphiné twinning (Fig. 12) and; (4) kinematic indicators mostly

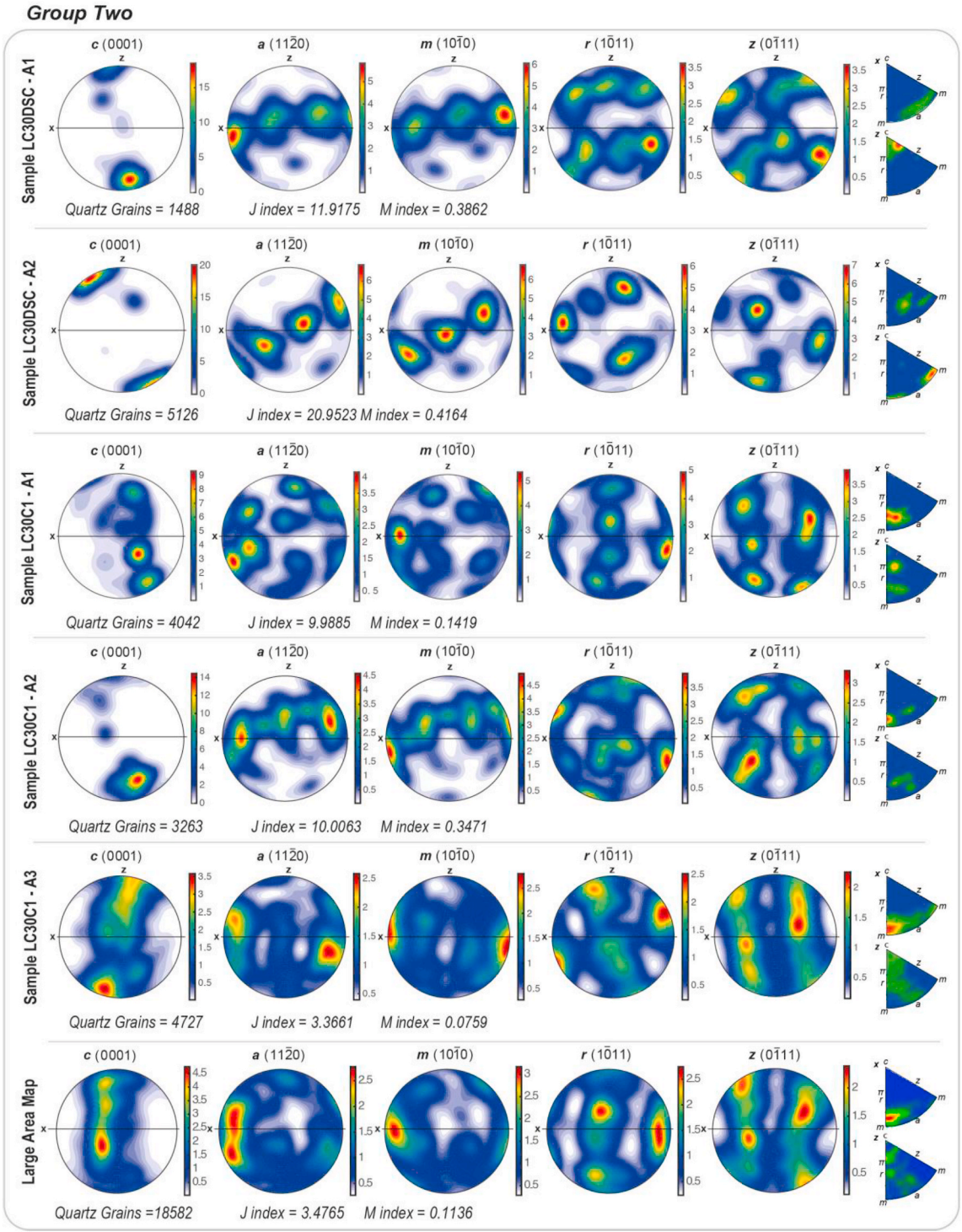

Fig. 10. Quartz crystallographic orientations for rocks from G2. Pole and Inverse pole figures (IPF). Pole figures are represented at lower hemisphere equal-area projections. IPFs are represented for X (upper right corner) and Z (lower right corner) directions. The densities of poles diagrams were color-coded and contoured in Multiples of a Uniform Distribution (M.U.D.), defined by the scale bar on the right of each pole figure. (For interpretation of the references to color in this figure legend, the reader is referred to the Web version of this article.)

consistent with sinistral sense of shear (Figs. 5–8). The composite quartz microstructures, which include (partially recrystallized) ribbons and grains, and matrix constituted of very fine-recrystallized grains, observed in most thin sections, are well documented in the literature for quartz deforming under greenschist conditions (e.g. Kjøll et al., 2015; Ceccato et al., 2017).

Quartzites and mylonite from G1 display old grains surrounded by smaller (~10 μm) recrystallized grains, mainly along serrated grain boundaries in quartz (Fig. 7h), and also along fractures in feldspar (Fig. 7g). This points to BLG (Fig. 13a) as the main dynamic recrystallization mechanism responsible for the intense grain-size reduction process, indicating temperature conditions around 400 °C (e.g. Schmid and Handy, 1991; Stipp et al., 2002b). In the case of feldspar from the mylonite, the small recrystallized grains could also be the result of

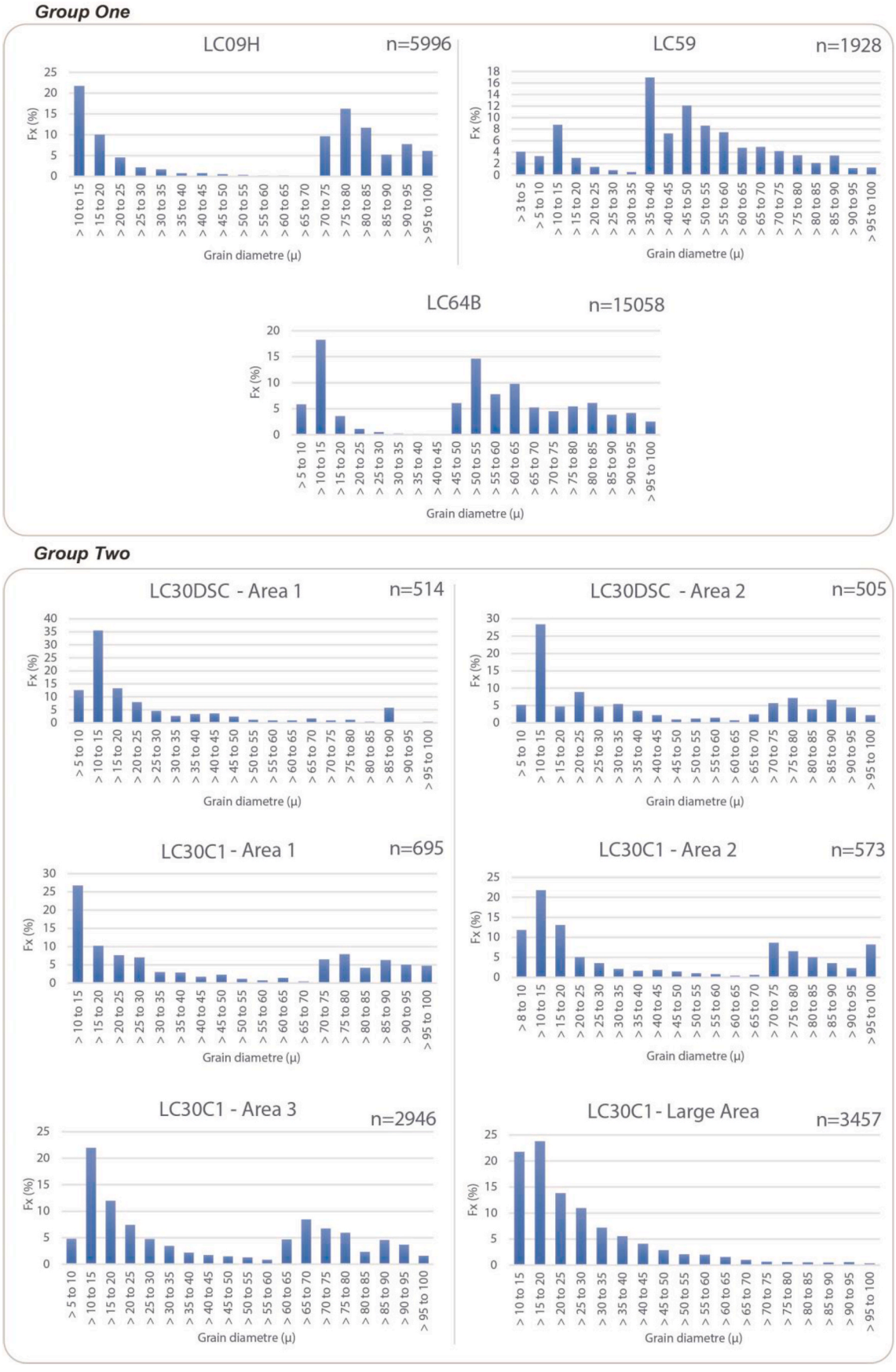

Fig. 11. Quartz grain-size frequency diagrams for samples from G1 and G2 (n = number of grains).

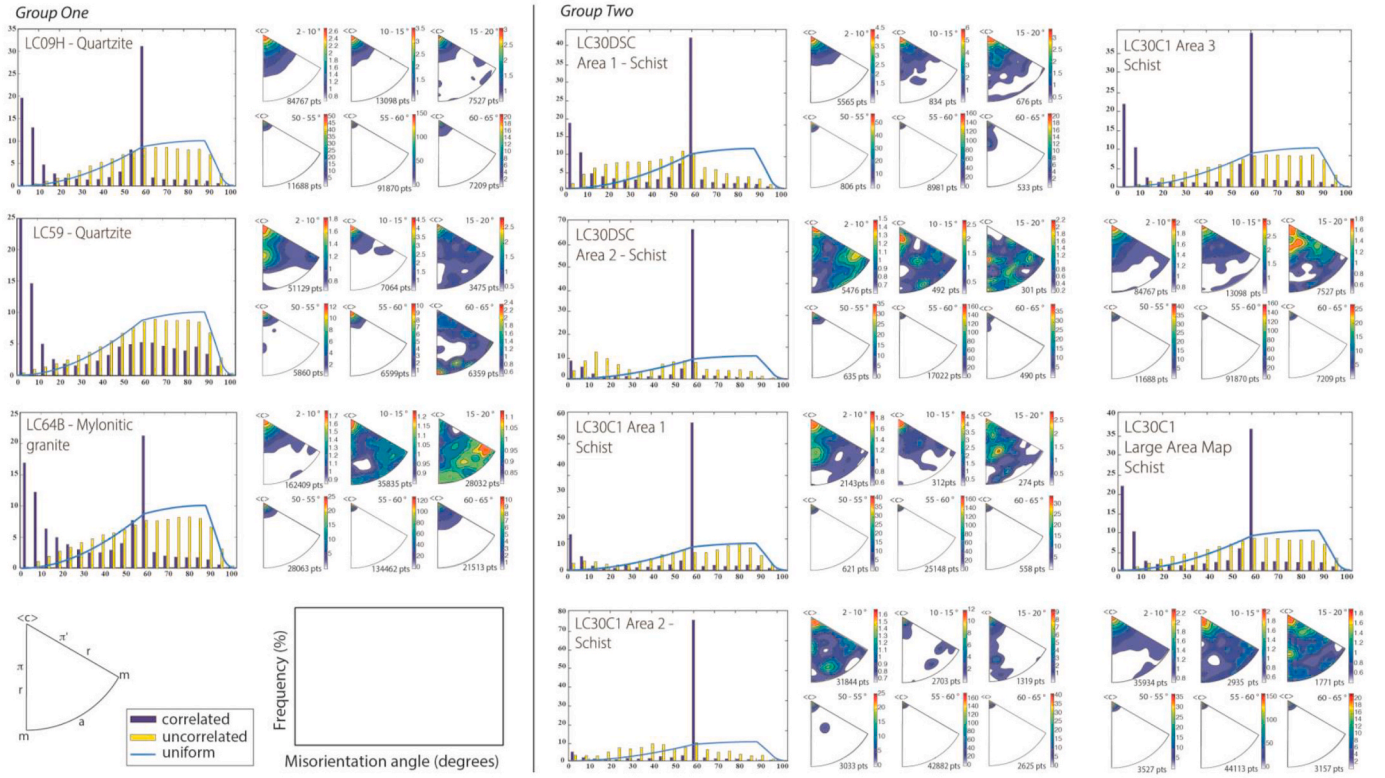

Fig. 12. Misorientation angle distribution histograms for quartz from samples from G1 and G2.

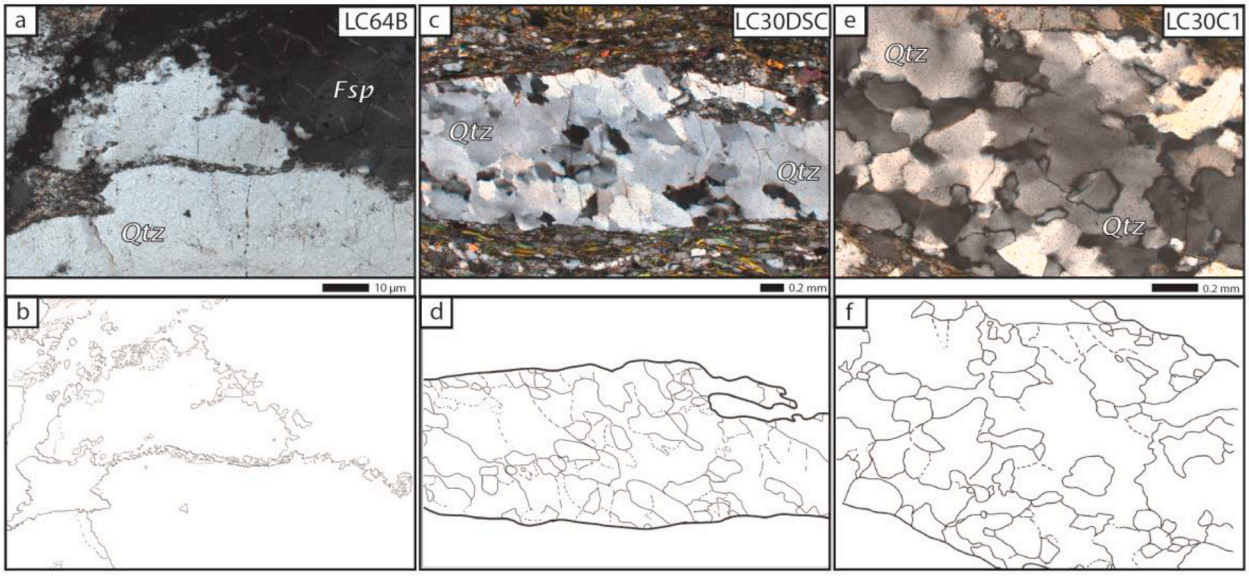

Fig. 13. Photomicrographs of the mylonitic granite (sample LC64B) from G1 and quartz schist from G2 (samples LC30DSC and LC30C1), and corresponding sketches displaying the main aspects of the intense recrystallization process. (a) and (b) Bulges and recrystallized small grains along the parent grain boundaries, indicating dominance of BLG recrystallization in the southern Lancinha shear zone. (c) and (d) subgrain boundaries oriented oblique to the foliation, suggesting SGR recrystallization and a slight temperature increase northwards along the Lancinha shear zone. (e) and (f) Irregular lobate grain boundaries and irregular amoeboid grain shapes suggesting GBM recrystallization and higher temperatures in the northern Lancinha shear zone.

classical nucleation, but differentiating whether these grains are the product of recrystallization by BLG or by classical nucleation is difficult, since both processes involve boundary migration (e.g. Fitz Gerald and Stünitz, 1993). Both classical nucleation and recrystallization by BLG, however, may occur at temperatures below 450 °C (e.g. Fitz Gerald and Stünitz, 1993), and given the presence of the hydrated assemblage in the mylonite (~10% of mica), which may enhance these processes, dynamic recrystallization of feldspar together with quartz is likely. Additionally, the presence of few quartz new grains with sizes close to the subgrains (Fig. 7e) suggests that quartzite (LC59) was also recrystallized by SGR to some extent.

Schists from G2 show S–C fabrics (Fig. 5b and c), garnet

porphyroblasts with recrystallized quartz in pressure shadows, and biotite fish, all suggestive of sinistral shear (Figs. 6 and 8). The schists also have aggregates of deformed plagioclase that exhibit deformation twins (Fig. 8e and f), quartz recrystallized grains with sizes up to ~200 μm, with 50–85% of grains up to 50 μm in diameter (being ~25% > 10–20 μm) in the EBSD mapped area, and significant evidence of SGR and GBM recrystallization (Fig. 13c, d, e, f). This evidence suggests that during sinistral shear-related dynamic recrystallization, rocks from G2 recrystallized by BLG and SGR, which lead to a decrease in grain-size, and by GBM, which lead to an increase in size of the recrystallized quartz grains, likely under higher temperature conditions (>400–500 °C; e.g. Stipp et al., 2002b) than the deformation recorded by the G1 rocks.

The occurrence of BLG recrystallization in rocks displaying evidence for operation of both SGR and GBM, suggests that rocks from G2 were first deformed at higher temperature conditions and later underwent lower temperature deformation, given that BLG recrystallization is not expected to occur under the same high temperatures at which GBM operates (e.g. Platt and Behr, 2011). Therefore, GBM likely represents an older preserved microfabric overprinted by a later BLG during exhumation. Such an overprinting relationship is common in large-scale shear zones with long-lasting deformation history (e.g. Means, 1995). BLG overprint on rocks first recrystallized by GBM has also been suggested by Faleiros et al. (2011) for residual neosones and mylonitic granitic leucosome (samples 137, 122 and 257 in their Fig. 3 and their Table 1) deformed close to the sinistral Serra do Azeite shear zone.

Schists with similar composition to the G2 schists immediately south of the town of Barra do Turvo, between the Putunã and Serra do Azeite shear zones, were recrystallized by GBM or both SGR and GBM (samples FM138, FM136 and 070 in Fig. 3 and Table 1 in Faleiros et al., 2011). Furthermore, considering the suggested recrystallization mechanisms operating during quartz recrystallization in the whole area studied by Faleiros et al. (2011), and the ones suggested here for the G2 rocks, a competition between SGR and GBM mechanisms, with some secondary overprint by BLG, seems to be a realistic scenario during dynamic recrystallization associated with the deformation in the northern of the LSZ, and at the Putunã and Serra do Azeite shear zones. Such a scenario implies similar deformation conditions for rocks deformed along these shear zones.

Texture analysis results, such as the strong concentration of <c> axes close to the Z direction (pole to foliation) plus the concentration of <a> axes parallel to X (stretching lineation) suggest that the basal <a> slip is the dominant slip system in the G1 quartzites LC09H and LC59 (Fig. 9). This slip system is typical for quartzites deforming under low-temperature conditions (e.g. Schmid and Casey, 1986; Hirth and Tullis, 1992; Stipp et al., 2002a), due to low-temperature dislocation creep (dislocation glide) deformation mechanisms (e.g. Hirth and Tullis, 1992). Evidence for dislocation creep in these rocks are intracrystalline deformation features such as undulose extinction, subgrain boundaries and deformation bands. Dislocation glide was certainly facilitated by intense dynamic recrystallization, given that under low temperature conditions, dislocation glide can only accommodate a small amount of strain before strain hardening and stress concentration lead to fracture (Davis et al., 2012). The asymmetric distribution of <c> axes (at ~30° counterclockwise from Z) indicates sinistral sense of shear and accommodation of non-coaxial deformation in the quartzites. Subsidiary deformation by slip on the system rhomb <a> may also have occurred, as there is some concentration of poles to {r} close to Z, also confirmed in the IPFs maps (e.g. Toy et al., 2008). It is difficult to infer slip systems from quartz texture in the mylonitic granite (sample LC64B), and we can only mention that during strain localization {z} planes were oriented favorable for sliding. However, the presence of some high-angle boundaries in the interval between >15 and 100° in the misorientation angle histograms for this sample (Fig. 12) suggests a transition from dislocation creep to dislocation accommodated grain boundary sliding (e.g. Miranda et al., 2016) or, alternatively, a transition from dislocation creep to fluid assisted (or dissolution-precipitation creep assisted) grain boundary sliding (e.g. Lagoeiro and Fueten, 2008), as recrystallization, irrespective of its mechanisms, would not produce such a wide range of angle distribution (Vernooij et al., 2006).

Small circles defined by quartz <c> axes are slightly oblique to Z in a counterclockwise sense (samples LC30DSC Area 1 and Area 2 and LC30C1 Area 2), suggesting activation of basal <a> slip and sinistral sense of shear (Fig. 9). Sinistral sense of shear can also be extracted from <c> axis distribution from sample LC30C1 Area 1. However, textural analysis for this sample shows quartz <c> axes distributed along a single girdle, which suggests a combination of multiple slip systems such as basal + rhomb along the <a> direction. Combined activity of basal <a> and rhomb <a> slip systems can also be inferred from quartz <c> axis fabric and IPFs from sample LC30C1 Area 3, and of rhomb <a> and prism <a> from the sample LC30C1 large area map, which has a concentration of <c> axis around the center of the pole figure (Fig. 10). Nevertheless, the <c> axis distribution along a broad single girdle skewed ~20° clockwise with respect to Z in the LC30C1 Area 3 suggests local dextral sense of shear, while a more symmetric distribution in the LC30C1 large area map can be related to a coaxial component of deformation. These observations point to strain partitioning at the sample scale during overall non-simple shear (e.g. transpressional) deformation. Furthermore, the presence of subgrain boundaries give microstructural evidence for crystal-plastic deformation (Passchier and Trouw, 2005), and suggests that the activation of multiple slip systems is due to dislocation creep deformation mechanism, likely involving dislocation climb at moderate temperature conditions. Dislocation creep deformation mechanism is also supported by the evidence of intracrystalline deformation in biotite, amphibole and plagioclase (Fig. 8).

All together, these data suggest that strain localization during the development of the Lancinha and associated shear zones was facilitated by intense grain-size reduction, as observed in many other shear zones elsewhere (e.g. Lloyd, 2004; Menegon et al., 2010; Platt and Behr, 2011). More specifically, while BLG is the dominating grain-size reducing mechanism in the southern region (G1 rocks), in the northern region (G2 rocks) SGR contributes significantly to the grain-size reduction process. In the northern region, GBM also might have contributed to the strain localization. Strain localization was certainly also facilitated by the pervasive development of Dauphiné twinning, as the presence of such twins reduces the strength of quartz and contributes to the grain-size reduction process (e.g. Lloyd, 2004; Stipp and Kunze, 2008; Menegon et al., 2010). This recrystallization evidence, the dominant asymmetry of <c> axis orientation observed in rock from both groups, plus the mainly activation of basal <a> slip in the southern region, and the combination of basal <a> + rhomb <a> + prism <a> in the northern region, is consistent with the interpretation presented above that strain localization occurred under temperatures of ~400 °C in the southern part and between >400 and 500 °C in the northern region, and involved a strong non-coaxial sinistral component during plastic deformation of the whole studied shear zone segment. It is worth noting that the suggestion of a slight increase in temperature towards the north of the LSZ is based on microstructural observations, mineral assemblage (biotite, K-feldspar, plagioclase, garnet, amphiboles in the north), and EBSD data from both group samples, and not only on the crystallographic fabrics. The crystallographic fabrics of sample LC30C1 from G2 show <c> axis distributed along girdles, some of them with maxima around Y. Such crystallographic fabrics, which suggest activation of rhombohedral and prismatic forms, could also result from a higher strain condition (e.g. Pennacchioni et al., 2010), as the temperature dependence for sliding along direction <a> has not been convincingly demonstrated (e.g. Kilian and Heilbronner, 2017). However, since we do not have any single Y maxima of <c> axis in our samples, a temperature of 500 °C seems to be a realistic maximum temperature estimate for deformation in the entire studied segment of the LSZ, given that the transition from combined basal, rhomb and prism <a> slip to dominant prism <a> slip, i.e. from YZ girdle distributions to

<c> axis Y maximum, likely occurs at 500 °C (Stipp et al., 2002a).

In summary, microstructural observations and textural analysis suggest that rocks from G1 recrystallized mainly by BLG and were deformed under temperature ~400 °C, with activation of basal <a> slip system. On the other hand, rocks from G2 likely recrystallized by SGR and GBM (with some later BLG recrystallization), and were deformed at >400–500 °C, with activation of multiple slip systems (basal <a>, rhomb <a> and prism <a>). Rocks from G1 in comparison with rocks from G2 have a higher amount of grains smaller than 50 μm, and are associated with strongly fractured feldspar with recrystallized grains along its fractures and margins. Rocks from G2 have larger amounts of recrystallized grains with sizes up 200 μm and are associated with plagioclase with deformation twins, and plastically deformed amphibole and biotite. The different microstructures, deformation mechanisms and temperatures show that the way these different rocks responded to deformation varied widely during the shear zone evolution. Such a variance could be due to differences in the amount of exhumation, the north portion of the studied segment representing a slightly deeper section through the LSZ. Alternatively, deformation may have continued for somewhat longer in the south during exhumation-related cooling. More microstructural data, especially in the south portion of LSZ, in combination with geochemical and geochronological analysis are necessary to better evaluate these alternatives.

5.2. Implications for the tectonic evolution of the ribeira belt

The tectonic evolution of the southern Ribeira belt, principally concerning the Curitiba terrain, has recently been interpreted as the result of a polyphase deformation history with six successive phases of deformation occurring from 600 to 580 Ma, with three of these (D3-D6) developing over a time period of only four million years (584-580 Ma; Faleiros et al., 2016). This interpretation was based on inclusions pattern in porphyroblasts (D1-D2) predated by the main foliation (D3), and mesoscopic to regional folding of the main foliation (D4-D5) with folds being flanked by shear zones (D6). Considering that we are dealing with an anastomosing interconnected shear zone system at a large-orogenic scale, with geometric complexities at a variety of scales, we would argue that much if not all of this deformation history may be the result of progressive orogenic deformation (e.g. Fossen et al., 2019). In this regard, Faleiros et al. (2016) also indicate that some of their six deformation phases could represent progressive deformation.

Another characteristic feature of many transpressional orogenic sections is the tendency for strain to partition into pure shear-dominated domains separated by strike-slip (dominated) shear zones that accommodate much or all of the simple shear displacement (e.g. Oldow, 1990; Tikoff and Teyssier, 1994). In many cases strain partitioning becomes more pronounced at late stages of deformation, and the progressive localization of shear into shear zones (D6 of Faleiros et al., 2016) could work in tandem with shortening by thrusting and folding (D4-D5) in the pure shear-domains between the shear zones. Such partitioned transpressional (and locally transtensional) deformation has been suggested further north, from geometrical construction along the Serra do Azeite shear zone in the Apiaí terrain (Dehler et al., 2007), and along the Taxaquara shear zone (Ribeiro et al., 2019), and for the Ribeira belt as a whole (Ebert and Hasui, 1998).

The above-mentioned strain partitioning occurs at the scale of tens of kilometers, but we also observe structural features that can be related to strain partitioning at smaller scales. The partitioning relates to rheologic differences down to the microscale, where micaceous layers behave different from quartzo-feldspatic layers. S–C structures are a particularly common type of small-scale strain partitioning structure, and microstructures also reveal differences in type of deformation or flow. While several samples show consistent sinistral flow, quartz-schists from G2 display quartz texture mainly suggestive of sinistral shear, but with a local more symmetric distribution and even an observation of local dextral sense of shear, as inferred from quartz <c> axis distributions (Fig. 10). This may be a microscale example of partitioning of transpression, where the pure shear component produces conjugate shear bands. Alternatively, such partitioning can be set up by local rheologic or geometric irregularities that produce local non-laminar flow, by slip on foliations (Harris and Cobbold, 1984) and by temporal flow variations (Hudleston, 1999). Common for all of these expressions of strain partitioning is that they would become more pronounced over time, as heterogeneities such as steep fold limbs and foliations develop. On a large scale, linkage of shear zone segments to form the observed anastomosing framework creates spatial variations in flow. Interestingly, similar patterns are seen at the microscale, where anastomosing patterns of phyllosilicates surround more quartzo-feldspatic lenses (Figs. 6b and 7c).

The consistent sinistral sense of shear found in this work contrasts with the dextral sense of shear loosely assigned to the Lancinha shear zone by previous workers (e.g. Faleiros et al., 2010, 2011, 2016). However, we have not been able to find actual evidence in support of such dextral sense of shear in the published literature. Unlike the dextral Ribeira shear zone to the northwest (Fig. 3), which exhibits clockwise rotation of foliation and lithologic contacts into the shear zone consistent with dextral shear, the Lancinha shear zone shows no such rotations clear enough to reveal its sense of shear. Hence, we will depart from the outcrop and microscale observations of sinistral sense of shear presented here.

The observed kinematics of the Lancinha shear zone conforms with the sinistral shear assigned to the Putunã and Serra do Azeite shear zones to the southeast (Fig. 2; Dehler et al., 2007; Faleiros et al., 2011, 2016). These two sinistral shear zones parallel the Lancinha shear zone, while the Ribeira shear zone to the northwest has a more easterly trend (Fig. 3). The difference in orientation (~20°) between the dextral Ribeira and the sinistral Lancinha, Putunã and Serra do Azeite shear zones is lower than what would be expected for a conjugate set, even when considering that in a transpressional setting, the pure shear component would lower the angle somewhat over time. Hence, we are probably facing a more complex kinematic picture that could in part be caused by kinematic complications along a composite anastomosing shear zone network affecting a rheologically heterogeneous portion of the crust. Lateral extrusion or escape of blocks between shear zones of similar orientations has been suggested (Faleiros et al., 2010, 2016). Lateral escape has also been discussed from many other orogenic belts worldwide, and this may be a feasible explanation for subparallel shear zones showing opposite kinematics. In the well-explored case of the Himalayan-Tibetan system, lateral escape or extrusion is generally explained in terms of indenter tectonics, with the old and rigid Indian crust representing a more rigid block than the Asian crust (e.g. Molnar and Tapponnier, 1975). In this context, we speculate that the Congo craton might represent such an indenter relative to a softer Brasilia-belt crust on the west side of the southern Ribeira belt.

Eroded sections through regions of extrusion tectonics settings are identified in several ancient orogenic settings, including the Paleoproterozoic Superior boundary zone in Canada (Kuiper et al., 2011), the Neoproterozoic of NE Brazil (Borborema Province; Araujo et al., 2014) and East Africa-Antarctica (Jacobs and Thomas, 2004). A particularly interesting and well-documented system is the Appalachian example described by Massey and Moecher (2013). Also here, subparallel dextral and sinistral shear zones unexpectedly coexist in an overall dextral transpressional orogenic setting. Geochronologic constraints, metamorphic and textural observations and structural relations demonstrate that the opposing shear senses and related structures were coeval. Furthermore, variations in structural patterns show that deformation was partitioned in a rather complex way, with zones of varying kinematic vorticity, lineation orientations and strain patterns. In this Appalachian example, the progressive deformation lasted for 30 m.y. (330-300 Ma; Massey and Moecher, 2013). In the Ribeira belt, the relevant deformation lasted for just a few million years (584-580; D3-D6 of Faleiros et al., 2016), which would normally be taken to represent a

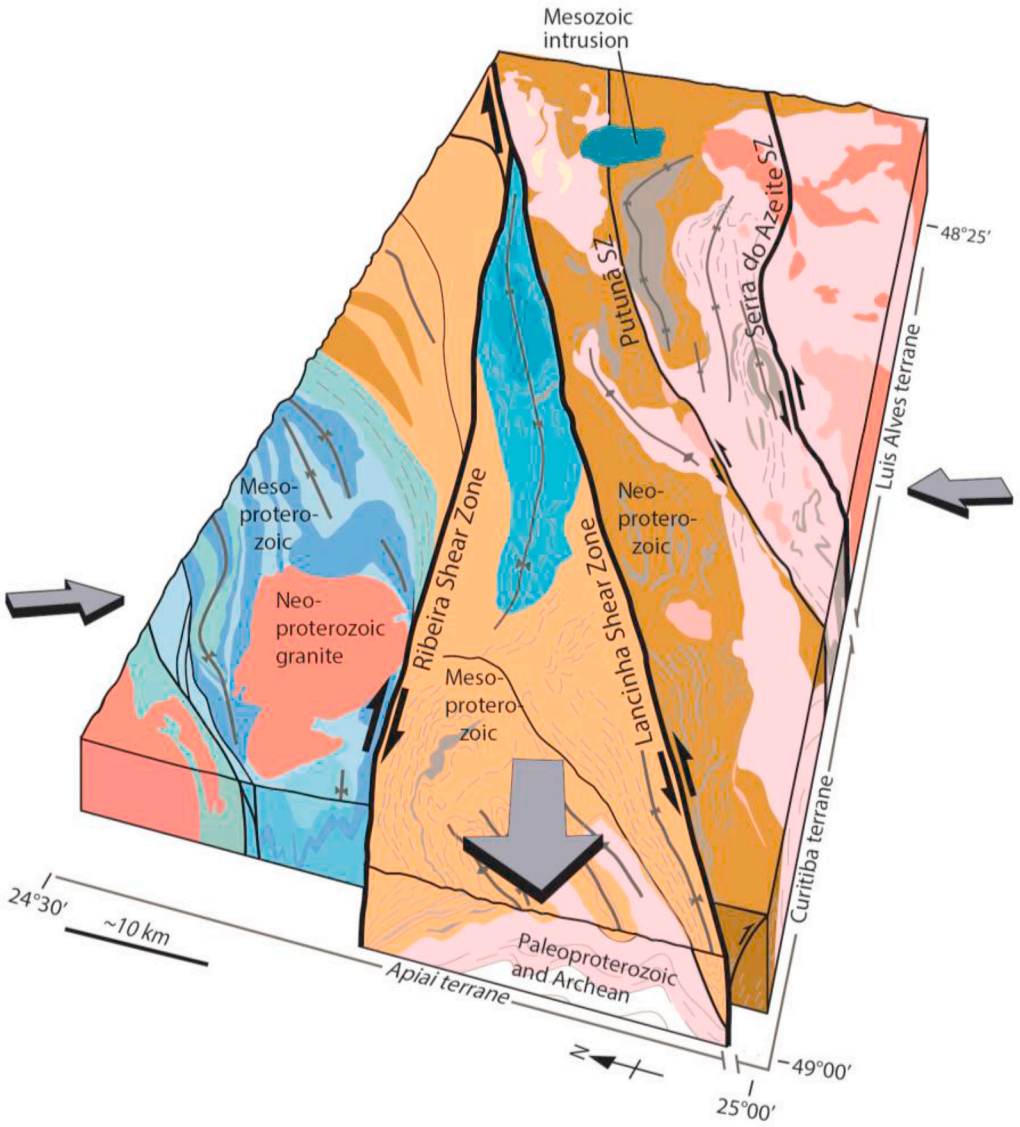

Fig. 14. Block diagram illustrating the southwestward escape of the block bounded by the Ribeira and Lancinha shear zones during transpressive orogenic shortening. Modified from Fossen et al. (2019). Colors roughly corresponding to Fig. 3. (For interpretation of the references to color in this figure legend, the reader is referred to the Web version of this article.)

single progressive deformation. Hence, it is reasonable to assume that the dextral and sinistral deformation represented by the shear zones in this region were coeval as well.

According to previous workers (Passarelli et al., 2011; Faleiros et al., 2011, 2016) the sinistral shear sense on the Lancinha shear zone is replaced by dextral shear to the northeast, in the segment known as the Cubatão shear zone. This could be related to dextral shear being taken up by the adjoining Ribeira shear zone, meaning that the block between the Ribeira and the Lancinha shear zones was extruding southwestward, as illustrated in Fig. 14. The result of such a progressive extrusion would be a zipper-style merging of the Ribeira and Lancinha shear zones as the extrusion proceeds, and possibly with a southwestward increasing effect of extrusion. More targeted kinematic analysis and deformation dating along the different segments of this intriguing shear zone system is needed to evaluate this model.

6. Conclusions

We have performed a detailed structural mapping and microstructural study and applied the SEM-ESBD technique to analyze the full crystallographic orientation of quartz grains in quartzites, mylonitic granite and quartz-schists that were intensely recrystallized during the development of the Lancinha Shear Zone in the anastomosing southern Ribeira belt shear zone system. Our study shows that:

1 Rocks were intensely recrystallized by BLG, especially in the southern portion of the Lancinha Shear Zone, and also by SGR and GBM in the northern portion. BLG and SGR seem to be the main recrystallization mechanisms responsible for grain-size reduction;
2 The plastic deformation along the LSZ is accommodated mainly by dislocation creep, with activation of basal <a> in the southern region and rhomb <a> + basal <a> and prism <a> in the northern region. The strain localization was facilitated by dynamic recrystallization due to BLG, SGR and GBM recrystallization, under temperature conditions at around 400 °C in the southern region, and at around >400–500 °C in the northern region, and by pervasive Dauphiné twinning;
3 The anastomosing pattern defined by interconnected shear zones observed at meso- and macroscale (Figs. 2 and 5) is also identified at

the microscale by the occurrence of S–C foliation and anastomosing foliation associated with flattened quartz grains (Figs. 6 and 7);

4 The analysis of a broad variation of shear sense indicators, such as biotite fish, S–C fabrics and rotated porphyroblasts, indicate predominantly sinistral sense of shear on the LSZ. This is also inferred from quartz <c> axis distribution, which have asymmetric girdles rotated counterclockwise to Z;

5 Our observations fit a general model for an overall dextral transpressional system for the Ribeira belt that involves lateral extrusion and dual sense of shear on shear zones, bounding extruding blocks during a progressive orogenic evolution.

6 The predominance of sinistral kinematic indicators, different from what has been superficially suggested in the recent literature (e.g. Faleiros et al., 2016), suggests that interpretation on kinematics and, consequently, tectonic evolution of such interconnected shear zone systems should be done with great care, especially in transpressional regimes involving strain partitioning. Further investigation involving dating of the plastic deformation is needed to better understand the significance of such a sinistral shear in an overall dextral orogenic setting.

Author statement (contributions)

Thailli Conte: Conceptualization, Methodology, Validation, Formal analysis, Investigation, Resources, Writing - Original Draft, Visualization, Carolina Cavalcante: Conceptualization, Methodology, Validation, Formal analysis, Investigation, Resources, Writing - Review & Editing, Visualization, Supervision, Project administration, Funding acquisition. Leonardo Lagoeiro: Resources, Writing - Review & Editing, Supervision, Funding acquisition. Haakon Fossen: Conceptualization, Methodology, Writing - Review & Editing, Visualization. Camila Silveira: Software, Formal analysis.

Declaration of competing interest

The authors declare that they have no known competing financial interests or personal relationships that could have appeared to influence the work reported in this paper.

Acknowledgments

TC wishes to thank the Coordenação de Aperfeiçoamento de Pessoal de Nível Superior-Brasil (CAPES) for the granting of the master's scholarship (Finance code 001). This work was partially funded by the Brazilian National Council for research and Technology Development (CNPq) via processes number 434202/2018-5 to CC, and 305232/2018-5 and 425412/2018-0 to LL. The manuscript was greatly benefited by the reviews of Alberto Ceccato and an anonymous reviewer. We are also grateful to Rheinhardt Fuck for careful editorial handling. We would like to thank Gustavo Viegas and Rhander Altoé, whose contributions helped to improve this work, and Rodrigo Santos for field assistance.

Appendix A. Supplementary data

Supplementary data to this article can be found online at https://doi.org/10.1016/j.jsames.2020.102750.

References

Araujo, C.E.G., Weinberg, R., Cordani, U., 2014. Extruding the borborema province (NE-Brazil): a two-stage neoproterozoic collision process. Terra. Nova 26, 157–168. https://doi.org/10.1111/ter.12084.

ASTM E2627-13, 2019. Standard Practice for Determining Average Grain Size Using Electron Backscatter Diffraction (EBSD) in Fully Recrystallized Polycrystalline Materials. ASTM International, West Conshohocken, PA, 2019.

Bachmann, F., Hielscher, R., Schaeben, H., 2010. Texture analysis with MTEX - free and open source software toolbox. Solid State Phenom. 160, 63–68. https://doi.org/10.4028/www.scientific.net/SSP.160.63.

Bento dos Santos, T., Tassinari, C., Fonseca, P., 2015. Diachronic collision, slab break-off and long-term high thermal flux in the Brasiliano-Pan-African orogeny: implications for the geodynamic evolution of the Mantiqueira Province. Precambrian Res. 260, 1–22. https://doi.org/10.1016/j.precamres.2014.12.018.

Berger, A., Herwegh, M., Schwarz, J.O., Putlitz, B., 2011. Quantitative analysis of crystal/grain sizes and their distributions in 2D and 3D., Journal of Structural Geology. https://doi.org/10.1016/j.jsg.2011.07.002.

Campagnoli, F., 1996. Considerações sobre a geologia da sequência Turvo-Cajati, na região do alto Rio Jacupiranguinha, SP. Dissertação de Mestrado. Inst. De Geociências, Universidade de São Paulo, São Paulo, p. 93.

Campanha, A.G.C., 2002. O papel do sistema de zonas de cisalhamento transcorrentes na configuração da porção meridional da Faixa Ribeira. Tese de Livre Docência. Universidade de São Paulo. https://doi.org/10.11606/T.44.2009.tde-16122009-094247.

Campanha, G.A.C., Faleiros, F.M., Basei, M.A.S., Tassinari, C.C.G., Nutman, A.P., Vasconcelos, P.M., 2015. Geochemistry and Age of Mafic Rocks from the Votuverava Group, Southern Ribeira Belt, vol. 266. Evidence for 1490 Ma oceanic back-arc magmatism, Brazil, pp. 530–550. https://doi.org/10.1016/j.precamres.2015.05.026. Precambrian Research.

Cavalcante, C., Lagoeiro, L., Fossen, H., Egydio-Silva, M., Morales, L.F.G., Ferreira, F., Conte, T., 2018. Temperature constraints on microfabric patterns in quartzofeldsphatic mylonites, Ribeira belt (SE Brazil). J. Struct. Geol. 115, 243–262. https://doi.org/10.1016/j.jsg.2018.07.013.

Ceccato, A., Pennacchioni, G., Menegon, L., Bestmann, M., 2017. Crystallographic control and texture inheritance during mylonitization of coarse grained quartz veins. Lithos 290–291. https://doi.org/10.1016/j.lithos.2017.08.005.

Davis, G.H., Reynolds, S.J., Kluth, C., 2012. Structural Geology of Rocks and Regions, third ed., p. 861

Dehler, N.M., Machado, R., Vasconcelos, C.S., 2000. Tectônica extensional oblíqua no sul do Estado de São Paulo. Rev. Bras. Geociencias 30, 699–706.

Dehler, N.M., Machado, R., Fassbinder, E., 2007. Shear structures in the Serra do Azeite Shear Zone, southeastern Brazil: transtensional deformation during regional transpression in the central Mantiqueira province (Ribeira Belt). J. S. Am. Earth Sci. 23, 176–192. https://doi.org/10.1016/j.jsames.2006.09.017.

Ebert, H.D., Hasui, Y., 1998. Transpressional tectonics and strain partitioning during oblique collision between three plates in the Precambrian of southeast Brazil. In: Holdsworth, R.E., Strachan, R.A. (Eds.), Continental Transpressional and Transtensional Tectonics, vol. 135. Geology Society, London, pp. 231–252. https://doi.org/10.1144/GSL.SP.1998.135.01.15. Special Publications.

Faleiros, F.M., Pavan, M., 2013. Geologia e Recursos Minerais da Folha Eldorado Paulista – SG-22-X-B-XI, Estado de São Paulo. Companhia de Pesquisa de Recursos Minerais, CPRM. Escala 1:100.000.

Faleiros, F.M., Campanha, G.A.C., Bello, R.M.S., Fuzikawa, K., 2010. Quartz recrystallization regimes, c-axis texture transitions and fluid inclusion reequilibration in a prograde greenschist to amphibolite facies mylonite zone (Ribeira Shear Zone, SE Brazil). Tectonophysics 485, 193–214. https://doi.org/10.1016/j.tecto.2009.12.014.

Faleiros, F.M., Campanha, G.A.C., Martins, L., Vlach, S.R.F., Vasconcelos, P.M., 2011. Ediacaran high-pressure collision metamorphism and tectonics of the southern Ribeira Belt (SE Brazil): evidence for terrane accretion and dispersion during Gondwana assembly. Precambrian Res. 189, 263–291. https://doi.org/10.1016/j.precamres.2011.07.013.

Faleiros, F.M., Morais, S.M., Costa, V.S., 2012. Geologia e Recursos Minerais da Folha Apiaí – SG.22-X-B-V – Estados de São Paulo e Paraná. CPRM- Serviço Geológico do Brasil. Escala 1:100.000.

Faleiros, F.M., Campanha, G.A.C., Pavan, M., Almeida, V.V., Rodrigues, S.W.O., Araujo, B.P., 2016. Short-lived polyphase deformation during crustal thickening and exhumation of a collisional orogen (Ribeira Belt, Brazil). J. Struct. Geol. 93, 106–130. https://doi.org/10.1016/j.jsg.2016.10.006.

Fitz Gerald, J.D., Stünitz, H., 1993. Deformation of granitoids at low metamorphic grade. I: reactions and grain size reduction. Tectonophysics 221, 269–297. https://doi.org/10.1016/0040-1951(93)90163-E.

Fossen, H., Cavalcante, G.C.G., 2017. Shear zones - a review. Earth Sci. Rev. 171, 434–455. https://doi.org/10.1016/j.earscirev.2017.05.002.

Fossen, H., Cavalcante, G.C.G., Pinheiro, R.V., Archanjo, C.J., 2019. Deformartion – progressive or multiphase? J. Struct. Geol. 125, 82–99. https://doi.org/10.1016/j.jsg.2018.05.006.

Harris, L.B., Cobbold, P.R., 1984. Development of conjugate shear bands during bulk simple shearing. J. Struct. Geol. 7, 37–44. https://doi.org/10.1016/0191-8141(85)90113-0.

Heilbronner, R., Tullis, J., 2006. Evolution of c axis pole figures and grain size during dynamic recrystallization: results from experimentally sheared quartzite. Journal of Geophysical Research, 111, B10202. https://doi.org/10.1029/2005JB004194.

Herwegh, M., 2000. A new technique to automatically quantify microstructures of fine grained carbonate mylonites: two step etching combined with SEM imaging and image analysis. J. Struct. Geol. 22, 391–400. https://doi.org/10.1016/S0191-8141(99)00165-0.

Hielscher, R., Schaeben, H., 2008. A novel pole figure inversion method: specification of the MTEX algorithm. J. Appl. Crystallogr. 41, 1024–1037. https://doi.org/10.1107/S0021889808030112.

Hirth, G., Tullis, J., 1992. Dislocation creep regimes in quartz aggregates. J. Struct. Geol. 14, 145–159. https://doi.org/10.1016/0191-8141(92)90053-Y.

Hobbs, B., Mühlhaus, H.-B., Ord, A., 1990. Special Publications. Instability, Softening and Localization of Deformation, vol. 54. Geological Society, London, pp. 143–165. https://doi.org/10.1144/GSL.SP.1990.054.01.15, 1.

Hudleston, P., 1999. Strain compatibility and shear zones: is there a problem? J. Struct. Geol. 21, 923–932. https://doi.org/10.1016/S0191-8141(99)00060-7.
Jacobs, J., Thomas, R.J., 2004. Himalayan-type indenter-escape tectonics model for the southern part of the late Neoproterozoic-early Palaeozoic East African-Antarctic orogen. Geology 32, 721–724. https://doi.org/10.1130/G20516.1.
James, D.E., Assumpção, M., 1996. Tectonic implications of S-wave anisotropy beneath SE Brazil. Geophys. J. Int. 126, 1–10. https://doi.org/10.1111/j.1365-246X.1996.tb05263.x.
Kilian, R., Heilbronner, R., 2017. Analysis of crystallographic preferred orientations of experimentally deformed Black Hills Quartzite. Solid Earth 8, 1095–1117. https://doi.org/10.5194/se-8-1095-2017.
Kjøll, H.J., Viola, G., Menegon, L., Sørensen, B.E., 2015. Brittle-viscous deformation of vein quartz under fluid-rich lower greenschist facies conditions. Solid Earth. https://doi.org/10.5194/se-6-681-2015.
Kuiper, Y.D., Lin, S., Böhm, C.O., 2011. Himalayan-type escape tectonics along the superior boundary zone in manitoba, Canada. Precambrian Res. 187, 248–262. https://doi.org/10.1016/j.precamres.2011.03.009.
Lagoeiro, L., Fueten, F., 2008. Fluid-assisted grain boundary sliding in bedding-parallel quartz veins deformed under greenschist metamophic grade. Tectonophysics 446, 42–50. https://doi.org/10.1016/j.tecto.2007.10.004.
Lister, G.S., Hobbs, B.E., 1980. The simulation of fabric development during plastic deformation and its application to quartzite: the influence of deformation history. J. Struct. Geol. 2, 227–247. https://doi.org/10.1016/0191-8141(80)90023-1.
Lister, G.S., Paterson, M., Hobbs, B.E., 1978. The simulation of fabric development during plastic deformation and its application to quartzite: the model. Tectonophysics 45, 107–158. https://doi.org/10.1016/0040-1951(78)90004-5.
Little, T.A., Hacker, B.R., Brownlee, S.J., Seward, G., 2013. Microstructures and quartz lattice-preferred orientations in the eclogite-bearing migmatitic gneisses of the D'Entrecasteaux Islands, Papua New Guinea. Geochemistry, Geophysics. Geosystems 14, 2030–2062. https://doi.org/10.1002/ggge.20132.
Lloyd, G.E., 2004. Microstructural evolution in a mylonitic quartz simple shear zone: the significant roles of dauphine twinning and misorientation. In: Alsop, G.I., Holdsworth, R.E., McCaffrey, K.J.W., Hand, M. (Eds.), Flow Processes in Faults and Shear Zones. Geological Society of London, vol. 224, pp. 39–61. https://doi.org/10.1144/GSL.SP.2004.224.01.04. Special Publications.
Machado, R., Dehler, N.M., Vasconcelos, P., 2007. $^{40}Ar/^{39}Ar$ ages (600-570 Ma) of the Serra do Azeite transtensional shear zone: evidence for syncontractional extension in the Cajati area, southern Ribeira belt. An Acad. Bras Ciências 79, 713–723. https://doi.org/10.1590/S0001-37652007000400011.
Machado, R., Philipp, R.P., Mcreath, I., Peucat, J.J., 2016. Geochemical and isotopic evidence for the petrogenesis and emplacement tectonics of the Serra dos Órgãos batholith in the Ribeira Belt, Rio de Janeiro, Brazil. J. S. Am. Earth Sci. 68, 187–204. https://doi.org/10.1016/j.jsames.2016.01.005.
Mancktelow, N.S., Pennacchioni, G., 2004. The influence of grain boundary fluids on the microstructure of quartz-feldspar mylonites. J. Struct. Geol. 26, 47–69. https://doi.org/10.1016/S0191-8141(03)00081-6.
Massey, M.A., Moecher, D.P., 2013. Transpression, extrusion, partitioning, and lateral escape in the middle crust: Significance of structures, fabrics, and kinematics in the Bronson Hill zone, southern New England, U.S.A. J. Struct. Geol. 55, 62–78. https://doi.org/10.1016/j.jsg.2013.07.014.
Means, W., 1995. Shear zones and rock history. Tectonophysics 247, 157–160. https://doi.org/10.1016/0040-1951(95)98214-H.
Menegon, L., Piazolo, S., Pennacchioni, G., 2010. The effect of Dauphiné twinning on plastic strain in quartz. Contrib. Mineral. Petrol. 161, 635–652. https://doi.org/10.1007/s00410-010-0554-7.
Miranda, E.A., Hirth, G., John, B.E., 2016. Microstructural evidence for the transition from dislocation creep to dislocation-accommodated grain boundary sliding in naturally deformed plagioclase. J. Struct. Geol. 92, 30–45. https://doi.org/10.1016/j.jsg.2016.09.002.
Molnar, P., Tapponnier, P., 1975. Cenozoic tectonics of Asia: Effects of a continental collision. Science 189 (4201), 419–426. https://doi.org/10.1126/science.189.4201.419.
Neumann, B., 2000. Texture development of recrystallised quartz polycrystals unravelled by orientation and misorientation characteristics. J. Struct. Geol. 22, 1695–1711. https://doi.org/10.1016/S0191-8141(00)00060-2.
Oldow, J.S., 1990. Transpression, orogenic float, and lithospheric balance. Geology 18, 991–994. https://doi.org/10.1130/0091-613(1990)018<0991:TOFALB>2.3.CO;2.
Passarelli, C.R., Basei, M.A.S., Wemmer, K., Sigajr, O., Oyhantçabal, P., 2011. Major shear zones of southern Brazil and Uruguay: escape tectonics in the eastern border of Rio de La plata and Paranapanema cratons during the Western Gondwana amalgamation. Int. J. Earth Sci. 100 (2–3), 391–414. https://doi.org/10.1007/s00531-010-0594-2.
Passchier, C., Trouw, R.A., 2005. Microtectonics, second ed., ISBN 978-3-540-29359-0.
Pennacchioni, G., Menegon, L., Leiss, B., Nestola, F., Bromiley, G., 2010. Development of crystallographic preferred orientation and microstructure during plastic deformation of natural coarse- grained quartz veins. J. Geophys. Res.-Sol. Ea. 115, B12. https://doi.org/10.1029/2010JB007674, 2010.
Platt, J.P., Behr, W., 2011. Grainsize evolution in ductile shear zones: Implications for strain localization and the strength of the lithosphere. J. Struct. Geol. 33, 537–550. https://doi.org/10.1016/j.jsg.2011.01.018.
Poirier, J.P., 1980. Shear localization and shear instability in materials in the ductile field. J. Struct. Geol. 2, 135–142. https://doi.org/10.1016/0191-8141(80)90043-7.
Price, G.P., 1985. Preferred orientations in quartzites. In: Wenk, H.R. (Ed.), Preferred Orientation in Deformed Metals and Rocks: an Introduction to Modern Texture Analysis. Academic Press, Inc., Orlando, pp. 385–406. http://hdl.handle.net/102.100.100/276454?index=1.
Ramsay, J.G., 1980. Shear zone geometry: a review. J. Struct. Geol. 2 (½), 83–99. https://doi.org/10.1016/0191-8141(80)90038-3.
Ribeiro, T.B.V., Faleiros, F.M., Campanha, G.A.C., Lagoeiro, L., Weinberg, R.F., Hunte, N. J.R., 2019. Kinematics, nature of deformation and tectonic setting of the Taxaquara Shear Zone, a major transpressional zone of the Ribeira Belt (SE Brazil). Tectonophysics 751, 83–108. https://doi.org/10.1016/j.tecto.2018.12.025.
Sadowski, G.R., 1991. A megafalha de Cubatão no Sudeste Brasileiro. Boletim IG-USP. Serie Científica 22, 15–28. https://doi.org/10.11606/issn.2316-8986.v22i0p15-28.
Schmid, S.M., Casey, M., 1986. Complete fabric analysis of some commonly observed quartz c-axis patterns. Geophys. Monogr. 36, 263–286. https://doi.org/10.1029/GM036p0263.
Schmid, S.M., Handy, M.R., 1991. wards a Genetic Classification of Fault Rocks: Geological usage and tectonophysical implications. In: Moller, D.W., Mckenzie, J.A., Weissert, H. (Eds.), To Controversies in Modern Geology. Academic Press, London, pp. 339–361.
Stipp, M., Kunze, K., 2008. Dynamic recrystallization near the brittle- plastic transition in naturally and experimentally deformed quartz aggregates. Tectonophysics 448, 77–97. https://doi.org/10.1016/j.tecto.2007.11.041.
Stipp, M., Stünitz, H., Heilbronner, R., Schmid, S.M., 2002a. The eastern Tonale fault zone: a 'natural laboratory' for crystal plastic deformation of quartz over a temperature range from 250 to 700 C. J. Struct. Geol. 24, 1861–1884. https://doi.org/10.1016/S0191-8141(02)00035-4.
Stipp, M., Stünitz, H., Heilbronner, R., Schmid, S.M., 2002b. Dynamic recrystallization of quartz: correlation between natural and experimental conditions. In: De Meer, S., Drury, M.R., De Bresser, J.H.P., Pennock, G.M. (Eds.), Deformation Mechanisms, Rheology and Tectonics: Current Status and Future Perspectives, vol. 200. Geological Society, London, pp. 171–190. https://doi.org/10.1144/GSL.SP.2001.200.01.11. Special Publications.
Tikoff, B., Teyssier, C.T., 1994. Strain modeling of displacement-field partitioning in transpressional orogens. J. Struct. Geol. 16, 1575–1588. https://doi.org/10.1016/0191-8141(94)90034-5.
Toy, V.G., Prior, D.J., Norris, R.J., 2008. Quartz fabrics in the Alpine Fault mylonites: Influence of pre-existing preferred orientations on fabric development during progressive uplift. J. Struct. Geol. 30, 602–621. https://doi.org/10.1016/j.jsg.2008.01.001.
Trompette, R., 2000. Gondwana evolution; its assembly at around 600Ma. Comptes Rendus de l'Académie des Sciences. Sciences de la terre et des planétes 330, 305–315. https://doi.org/10.1016/S1251-8050(00)00125-7.
Vernooij, M.G.C., den Brok, B., Kunze, K., 2006. Development of crystallographic preferred orientations by nucleation and growth of new grains in experimentally deformed quartz single crystals. Tectonophysics 427, 35–53. https://doi.org/10.1016/j.tecto.2006.06.008.
Wenk, H.-R., Janssen, C., Kenkmann, T., Dresen, D., 2011. Mechanical twinning in quartz: Shock experiments, impact, pseudotachylites and fault breccias. Tectonophysics 510, 69–79. https://doi.org/10.1016/j.tecto.2011.06.016.
Wheeler, J., Prior, D.J., Jiang, Z., Spiess, R., Trimby, P.W., 2001. The petrological significance of misorientations between grains. Contrib. Mineral. Petrol. 141, 109–124. https://doi.org/10.1007/s004100000225.